# Challenges in Approaching the Detection Limits for Hillslope Erosion Using Terrestrial Laser Scanning

**A Thesis Presented for the**

**Master of Science**

**Degree**

**The University of Tennessee, Knoxville**

**Gene Nathan Bailey III**

**May 2022**

# DEDICATION

*To my wife Courtney Bailey for her love, patience, and support*

*To my advisor Dr. Yingkui Li for his guidance, care, and encouragement*

# ACKNOWLEDGEMENTS

I would like to extend my sincerest gratitude to my thesis committee, Dr. Yingkui Li, Dr. Daniel Yoder, and Dr. Hannah Herrero. Dr. Li enabled this journey and helped me all along the way with kindness, patience, and positivity. Dr. Yoder gave me confidence to learn things I assumed were out of my reach and was a great help throughout my research. Dr. Herrero always believed in me, made research more approachable, and saved me untold hours by recommending Zotero!

I want to thank the lecturers whom I had the pleasure to work with as a GTA. Drs. Kerr, Ellis, Teale, and Roman-Rivera were all supremely pleasant to work under and were all passionate educators with a heart for physical geography. Many thanks to Dr. Horn who provided opportunities to work on a very interesting project and make some extra money. I give thanks to the many GTAs I worked alongside. Our collaborations made me a more confident and capable lab instructor.

Thank you to my peers in GeoGrads, my friends, family, soccer teams, and countless others outside the university that made life much more fun. My deepest gratitude and love to Courtney. You were there for every step and I would certainly not be here without you.

# ABSTRACT

Accurately quantifying soil loss due to water erosion is a critical step in managing soils. Terrestrial LiDAR (Light Detection and Ranging) presents a potential alternative to traditional soil loss measurement by estimating soil erosion and deposition through detecting surface changes. Terrestrial LiDAR can also provide spatial distribution information without disturbing the observed surface. While erosion estimation through terrestrial LiDAR detects large magnitude erosion well, the finer temporal/spatial scale erosion experienced on the hillslope in sheet and rill erosion has remained a challenge to detect. This research addresses two of the challenges in using terrestrial LiDAR on fine scales in two manuscripts.

Chapter One presents Las2DoD, a new method for quantifying uncertainty in surface change analysis by operating directly on point clouds produced by terrestrial LiDAR. The theory of Las2DoD is given and supported by a case study of two erosion plots in comparison to two existing uncertainty analysis methods. The methods are compared with collected sediment delivery data to evaluate the effects of the uncertainty analysis methods in the context of measuring soil erosion. Las2DoD generated the most accurate estimate on both plots, capturing 90% and 65% of the measured sediment delivery, with the second-best performing method measuring 70% and 48%. Las2DoD also managed to preserve more low-magnitude changes relative to the other methods, which is particularly important when measuring small spatiotemporal scale changes.

In the second chapter, terrestrial LiDAR scans of an erosion plot while bare and vegetated are differenced to produce a very dense testing dataset. This dataset is used to assess the performance of three point cloud filtering algorithms, namely, a cloth simulation algorithm, a slope-based filter, and a random forest classifier. The methods are tested against a subset of the testing dataset using different sets of input parameters to identify optimum parameters. The highest-performing implementations of the filtering methods are then applied to the entire testing dataset and compared with one another. The

cloth simulation filter achieved the best classification, though the classification was highly influenced by parameter values that differed from established recommendations.

## TABLE OF CONTENTS

# LIST OF TABLES

# LIST OF FIGURES

# INTRODUCTION

## Hillslope Erosion

Soil fulfills many critical functions in an ecosystem. Among its many direct and indirect effects, soil acts as a medium for biological growth, a water filtering system, a carbon storage vector, and a nutrient cycling mechanism [1]. Excessive erosion impairs the soil's performance of these on-site functions and, on a global scale, is considered the most significant threat to the function of soils [2]. Soil erosion also induces detrimental off-site effects. Eroded sediment can transport pollutants to water systems, degrade aquatic habitats, reduce agricultural productivity, and cause sedimentation in reservoirs [3,4].

Hillslopes occupy the highest position in a watershed. Extending from the watershed divide to where water flow becomes concentrated, hillslopes generally cover the vast majority of surface area in a watershed. Since sediments eroded from the hillslope flow into channels further downslope and can be a substantial sediment source in a watershed [5], the hillslope is frequently the watershed position where erosion control is most effective and easily accomplished. Erosion at the upper portion of a hillslope is dominated by detachment through raindrop impact and transport through shallow flow. This process is known as sheet flow or interrill erosion when occurring between rills [6]. As water flows down the hillslope, small microchannels called rills are formed. In rills, the shear force of flowing water is the primary cause of detachment, and the flow itself provides transport [7]. Gullies are another feature of water erosion on hillslopes. Gullies are linear channels where runoff concentrates and removes soil to greater depths than rills. Unlike rills, gullies often reoccur in the same positions over time [8]. Gullies are typically classified as ephemeral and permanent (or classical) gullies. Ephemeral gullies are smaller than classical gullies and are distinguished from classical gullies in that ephemeral gullies can be obliterated through a disturbance like tilling [9].

## Erosion Measurement

The quantification of erosion by water is an essential step in assessing the impact of erosion and practices for reducing erosion. Many studies have asserted the importance of measuring erosion rates across scales [10–13]. Long-term erosion measurement is also needed to accurately capture extreme erosion events significantly affecting watersheds [14]. Garcia-Ruiz et al. [15] explicitly suggest erosion rate study periods of 20-25 years to reduce uncertainty in measuring erosion rates and better account for extreme events.

A variety of methods have been used to estimate erosion rates. Measuring sediment loss using bounded runoff plots began in the United States as early as 1917 and is still frequently practiced [16]. An experimental plot is isolated from outside movements of water and sediment. Under natural or simulated rainfall, a collection system captures sediments eroded from the plot for measurement. While bounded runoff plots can produce direct and accurate erosion estimates, those estimates should only be considered applicable to the scale and conditions the plot represents [17,18]. Measuring erosion in this way also provides little information about how eroded material is distributed spatially within the plot[14].

Estimating soil erosion by water through modeling is another common practice. Empirically-derived models like the Universal Soil Loss Equation and its derivatives estimate erosion through the best-fit analysis data collected from field plots [19]. Models built upon plot scale data often suffer the same downside as the plot data they are built upon, namely, loss of precision at the field scale relative to field observations [20]. In contrast, process-based models like the Water Erosion Prediction Project seek to estimate erosion by modeling fundamental mechanisms of water erosion [21]. The large amount of data required by process-based models is a limiting factor in their application [22].

A third approach to estimating soil erosion is monitoring in-field. On the scale of the hillslope, this could take a variety of forms, from measuring the surface change of gullies with the movement of erosion pins [23–25] to measuring the volume of eroded soil in rills and gullies [26].

Estimating erosion from the surface changes of rills or gullies is problematic because it does not account for sediments originating in interrill erosion areas, which Govers and Poesen [27] found to contribute as much as 46% on a tilled bare plot. Measuring deposition to estimate erosion rate relies on knowing the trapping efficiency of the feature that caused the deposition. This trapping efficiency can be challenging to assess and will change over time [28]. Many of these survey methods are lacking in spatial coverage and often involve disruptive or laborious practices in the field [29].

## Topographic Surveying for Measuring Erosion

As a potential alternative to the traditional plot and field measurement techniques, non-contact topographic surveying offers the three-dimensional (3D) measurement of a topographic surface without disrupting the soil. Since unsustainable amounts of erosion can manifest in millimeter-level surface changes, estimating erosion through topographic surveying requires extreme precision. For example, a soil's soil loss tolerance is defined as the greatest mass of soil that can be lost while maintaining the soil's productivity indefinitely [19]. The National Resource Conservation Service of the United States defines a maximum soil loss tolerance of 5 tons/acre/year. Assuming a soil bulk density of 1.4 g/cm$^3$, 5 tons of soil eroded uniformly over 1 acre would result in a surface elevation lowering of approximately 0.8 mm.

Photogrammetry and laser scanners are the two most common tools used in conducting non-contact surveying. Photogrammetry creates a 3D surface by stitching together images of a surface taken at different positions. Broadly, photogrammetric methods are classified as stereo-photogrammetry and Structure-from-Motion (SfM) photogrammetry. While both methods create structure through triangulating common features between images, traditional stereo-photogrammetry is different in that it requires knowledge of the position and orientation of the image-capturing device. Berger et al. [30] used stereo-photogrammetry at the laboratory-scale to study the development of rills under simulated rainfall. Stereo-photogrammetry has also been used aerially to monitor short-term gully erosion [31]. In SfM photogrammetry, the position and orientation of the image-capturing device are determined using automatically extracted features from the overlapping images in an iterative bundle adjustment procedure [32]. Using at least forty images taken from consumer-grade cameras, Hansel et al. [33] found SfM photogrammetry to adequately replicate soil loss estimations from rainfall simulations on an experimental plot. On a larger scale, Javernick et al. [34] applied SfM to images gathered by helicopter to generate elevation models of two kilometer-scale braided stream networks. SfM is much simpler to operate due to recent computer vision advances and freely available SfM software [35]. SfM also has the benefit of using the imagery acquired by Unmanned Aerial Vehicles (UAV).

The combination of UAV and SfM is used to estimate erosion through changes in a soil's surface. For example, Meinen & Robinson (2020) quantified erosion rates on an agricultural field using UAV-based SfM and correlated higher crop yields with lower erosion rates. Kaiser et al. [37] used SfM on UAV imagery to investigate nonerosive surface changes at the hillslope scale and cautioned that nonerosive processes should be considered when estimating erosion through surface changes. Eltner et al. [38] used UAV and SfM to detect systematic errors in plot surfaces measured by laser scanning and, after joining the laser and UAV data, measured soil surface changes. UAV and SfM also allow for large areas to be monitored. For example, Neugrig et al. [39] estimated erosion from surface changes for a 125,000 $m^2$ catchment.

Light detection and ranging (LiDAR) systems emit laser pulses, receive their reflection, and utilize the time-of-flight principle to measure topography with high precision [40]. LiDAR is most frequently used onboard aircraft, known as airborne LiDAR, or mounted on a tripod at the surface, known as Terrestrial Laser Scanning (TLS). TLS is of greater use to studies of erosion at the hillslope scale due to its ability to produce extremely dense point clouds and capture vertical surfaces with greater precision. TLS frequently appears in literature estimating erosion and deposition at various scales. Perroy et al. [41] found TLS to produce gully erosion estimations on-par with field measurements. Höfle et al. [42] leveraged GIS in combination with TLS to delineate gully features, and Li et al. [43] quantified sediment redistribution within gullies using TLS. Relative to airborne LiDAR, TLS is more suitable for detecting minor surface changes within gullies [44]. On the field-plot scale, TLS-derived surfaces and erosion estimations have been used to examine the structural and sedimentological connectivity of channels [45]. Though Lu et al. [46] found TLS adequate for measuring rill erosion, the authors noted that greater control over errors is needed to precisely measure interrill erosion. Similarly, Eltner and Baumgart [47] found TLS to reliably detect surface changes greater than 1.5 cm if error sources are carefully considered.

While TLS can measure large-magnitude erosion relatively simply [43,48,49], measuring the small-magnitude erosion on hillslopes challenges the system's resolution capability [28,45,46]. Several considerations are made to increase the capabilities of TLS at fine resolutions. Multiple scans are collected from different angles around the target of interest and then merged together to increase the point density and reduce the chances of missing any data [41,50]. When joining multiple scans, especially multitemporally, careful planning and attention must be paid to how the scans are registered together to reduce the measurement uncertainty as much as possible [47,51,52]. In merging multiple TLS scans, standard planar or spherical targets are often used to create spatially steady locations between scans. These common targets are then used to calculate the registration transformation between scans [53]. To minimize registration error as much as possible, targets are spatially distributed evenly within the scanning area while maintaining moderate overlap relative to planned scanning positions. Individual scans must have at least three common targets to calculate a valid registration [54].

After scans are registered into a common coordinate system, various methods may estimate the topographic change between point clouds. The most common method grids two point clouds into separate digital elevation models (DEM), which are subtracted from one another to produce a third DEM representing vertical topographic change. This method is known as the DEM of difference (DoD) [55]. When representing a point cloud surface by gridding, the grid resolution must be considered. A coarser grid resolution will reduce the influence of noise in the point cloud but reduces the detection precision of smaller topographic changes, whereas a finer grid resolution will better capture small spatial changes but increases the influence of erroneous points and can create gaps in the DEM where point density is lower [46,56]. The DoD method also benefits from a relatively simple uncertainty estimation using the roughness, which is the standard deviation of points that fall within each grid cell [55,57].

Other common methods avoid gridding and instead estimate topographic change by operating directly on the point cloud. A cloud-to-cloud (C2C) comparison calculates the distance between a point in one point cloud and the nearest point in the second point cloud. While this method is fast and straightforward, it is very sensitive to outlier points and does not give accurate measurements if the point cloud is not very dense [58]. Lague et al. [52] developed the multiscale model to model cloud comparison (M3C2) algorithm, which addresses some of the limitations of the C2C comparison. The M3C2 algorithm computes distances between two clouds along a normal surface direction and provides a confidence interval for each measurement based on registration error and point cloud roughness. Nourbakhshbeidokhti et al. [59] compared the DOD, C2C, and M3C2 methods and recommended the DOD method for estimating volumetric changes. They do note that the M3C2 method estimates topographic change more reliably when the topography is complex, as the method does not interpolate the surface.

## Point Filtering

At small spatiotemporal scales, interpretations of the soil surface are very sensitive to erroneous points. The filtering of non-soil, noise, and vegetation points is critical when performing analysis on LiDAR-generated surfaces. At fine resolutions, non-ground filtering has been found to significantly improve accuracy [60,61]. An approach often taken in TLS erosion studies is to manually determine non-soil points and filter them by hand [36,39]. Eltner et al. [38,47] mix manual and autonomous methods by using the CANUPO vegetation filter [62], which requires manual training data, and further filtering the results based on spatial statistics available in the open-source Point Cloud Library [63]. Due to the large number of scans present in multitemporal TLS erosion studies, these studies can significantly benefit from point filtering that is repeatable with as little user input as possible [64].

Many automatic LiDAR filtering methods have been developed and can be broadly thought of as surface-based, slope-based, and mathematical-morphology-based. Surface-based filtering defines a 3D region around minimum points in a neighborhood and iteratively classifies points as ground within the 3D region. Zhang et al.'s [65] cloth simulation filter (CSF) is an example of a surface-based method. The CSF filter inverts a point cloud and drapes a 'cloth' over the points. Gravity and the cloth's rigidity determine where the cloth falls, and points within a set distance of the cloth are considered ground points.

In slope-based filtering, the height and slope between points are calculated, and if outside of a defined threshold, the higher point is deemed non-ground. Vosselman [66] developed a slope-based filtering algorithm where the ground elevation differences between points are first normalized with a white top-hat transformation before calculating the slope and height between a given point and its neighbors. This slope-based method depends upon appropriately set slope and height thresholds, which necessitates some knowledge about the studied surface. Slope-based filters have been found to perform well on relatively flat surfaces but lose accuracy as the slope of a surface increases [67].

Mathematical-morphology-based filtering identifies non-ground points by performing closing and opening operations on point elevations relative to a minimum point within a window [68]. The window is then moved over the entire scan. The moving window size is highly influential on the performance of mathematical-morphology-based algorithms [69]. Zhang et al. [70] addressed this limitation by iteratively increasing the window size and filtering points based on elevation differences between the original surface and the morphologically opened surface. The algorithm assumes a constant slope for all of the scans, which can cause erroneous filtering on complex surfaces [65].

Roberts et al. [71] analyzed how several completely programmatic ground filtering algorithms performed on manually classified TLS reference datasets and found none of the algorithms suitable for all conditions represented by the reference dataset.

## Research Objectives

The goal of this thesis research is to address specific challenges in approaching the detection limits of TLS for measuring hillslope erosion. As highlighted by the reviewed literature, estimating surface changes from TLS is a complex task, presenting many research opportunities. Two facets of that task are explored here: uncertainty analysis and point cloud filtering. Specifically, the following questions are addressed:

- Can uncertainty quantification in DoD analysis of dense point clouds be improved by utilizing information inherent to dense point clouds to produce spatially varied uncertainty estimates without additional data?
- Can automatic point cloud filtering algorithms effectively remove non-soil points from a high-density fine-scale TLS dataset?

This thesis is organized in a manuscript format. The following two chapters are each a manuscript addressing one of the stated research objectives. Chapter 1 is entitled "Las2DoD: Change Detection Based on Digital Elevation Models Derived from Dense Point Clouds with Spatially Varied Uncertainty". This chapter presents a new approach to quantifying uncertainty within a DoD analysis performed on dense point clouds. Chapter 2, "Comparison of Ground Point Filtering Algorithms for Fine Spatial Resolution Erosion Studies Using Terrestrial LiDAR", examines the performance of several point cloud filtering algorithms using an automatically classified, highly dense TLS dataset. Following Chapter 2, the Conclusion section summarizes the major findings of this work, points out limitations and provides future research directions.

# CHAPTER I

# LAS2DOD: CHANGE DETECTION BASED ON DIGITAL ELEVATION MODELS DERIVED FROM DENSE POINT CLOUDS WITH SPATIALLY VARIED UNCERTAINTY

A version of this chapter was published by Gene Bailey, Yingkui Li, Nathan McKinney, Daniel Yoder, Wesley Wright, and Robert Washington-Allen:

Gene Bailey, Yingkui Li, Nathan McKinney, Daniel Yoder, Wesley Wright, Robert Washington-Allen. "Las2DoD: Change detection based on digital elevation models derived from dense point clouds with spatially varied uncertainty." *Remote Sensing* (2022): 14(7), 1537; https://doi.org/10.3390/rs14071537.

This paper has been published by the journal "Remote Sensing" as a part of the Spatial-Temporal Monitoring of Environmental and Ecological Processes Using LiDAR special issue. I wrote the original paper. The paper was edited by Yingkui Li, Daniel Yoder, and Wesley Wright. Yingkui Li, Nathan McKinney, and I collected the LiDAR data. Daniel Yoder and Wesley Wright collected and processed the sediment delivery data. Wesley Wright collected and processed the soil bulk density data. I processed and analyzed the LiDAR data. I developed the method, wrote the codes, and created most figures and tables.

## Abstract

The advances of remote sensing techniques allow for the generation of dense point clouds to detect detailed surface changes up to centimeter/millimeter levels. However, there is still a need for an easy method to derive such surface changes based on digital elevation models generated from dense point clouds while taking into consideration spatial varied uncertainty. We present a straightforward method, Las2DoD, to quantify surface change directly from point clouds with spatially varied uncertainty. This method uses a cell-based Welch's t-test to determine whether each cell of a surface experienced a significant elevation change based on the points measured within the cell. Las2DoD is coded in Python with a simple graphic user interface. It was applied in a case study to quantify hillslope erosion on two plots: one dominated by rill erosion, and the other by sheet erosion, in southeastern United States. The results from the rilled plot indicate that Las2DoD can estimate 90% of the total measured sediment, in comparison to 58% and 70% from two other commonly used methods. The Las2DOD-derived result is less accurate (65%) but still outperforms the other two methods (30% and 48%) for the plot dominated by sheet erosion. Las2DoD captures more low-magnitude changes and is

particularly useful where surface changes are small but contribute significantly to the total surface change when summed.

## Introduction

The advances of remote sensing techniques have allowed for the generation of very high-resolution digital elevation models (DEMs) for detecting surface changes up to centimeter/millimeter levels. Light detection and ranging (LiDAR) is a technology to create high-precision three-dimensional (3D) point clouds by measuring the time of flight of a laser point between a sensor and a surface [40]. It has been used aboard aircraft, commonly called airborne LiDAR, to produce DEMs with resolutions up to 0.5 m and coverages from a single to hundreds of kilometers [72–74]. Terrestrial laser scanning (TLS) is another type of LiDAR with laser scanners atop tripods near the area of interest and can produce denser point clouds with precision and resolution up to centimeter and millimeter levels. TLS has been used to survey smaller areas for change detection, such as the changing soil surfaces of gullies [41–44,48], hillslopes [47,75–77], bluffs [51], badlands [49], channels [57], experimental erosion plots [78], and tilled soils [79–81].

Structure from motion (SfM) is a widely used technology that uses cameras to produce dense point clouds for change detection. Based on an iterative bundle adjustment on automatically extracted key points, SfM generates point clouds from overlapping images without requiring a priori knowledge of the 3D position of each image [32,82]. While SfM can operate using images from ground-based cameras [82,83], unmanned aerial vehicles (UAVs) offer a low-cost image acquisition method with greater spatial and temporal resolutions. Leveraging images collected from UAVs, SfM has been used to quantify the surface changes of agricultural fields [36], hillslopes [37], catchments [39], glaciers [84], gorges [85], and experimental erosion plots [78].

Both LiDAR and SfM generate dense point clouds of the targeted surface. Surface changes can then be quantified based on the differences of the point clouds collected at different times. Two categories of analyses have been used for surface change detection: the 3D distance between point clouds and the difference of DEMs derived from point clouds. For the first category of analyses, a cloud-to-cloud (C2C) distance is the most straightforward method to quantify surface changes. This method derives an unsigned distance between each point of one cloud and the corresponding nearest point in the other cloud [86]. While the C2C approach is computationally and theoretically straightforward, the unsigned distances that result do not distinguish between positive (deposition) and negative (erosion) changes and do not account for the point clouds' positional uncertainty. This method also does not consider surface normals and yields reduced accuracy with increasing topographic complexity [52,59]. Lague et al. [52] developed a more robust surface distance method called the Multiscale Model to Model Cloud Comparison (M3C2) algorithm. This algorithm measures the distance between two point clouds by fitting a cylinder around each core point along the local surface normal direction and calculating the average point distance from the two point clouds within the cylinder. The normal direction and standard deviations of the points within the cylinder are used to derive surface roughness and, alongside a reported registration error, estimate a spatially variable confidence interval for uncertainty. While this technique avoids the potential for error propagation associated with gridding/interpolating surfaces and offers confidence intervals for point distances, it has trouble converting distances to volume change between surfaces surveyed several times [59].

Surface changes have been quantified primarily based on DEMs due to the simple concept, easy implementation, and straightforward visualization, though it is challenging to use DEMs to represent complex surfaces, such as overhanging and nearly vertical slopes [52,75,76,87]. The most common approach is to conduct a DEM of difference (DoD) that estimates the cell-by-cell elevation change between the DEMs of an area surveyed at successive times [55]. DEMs can be created from point clouds by gridding the area and summarizing the elevations of the points falling within each cell. DoDs can be used to quantify erosion and deposition on bare soil surfaces and to estimate volume change.

A DEM-represented surface usually contains uncertainties from sampling, gridding, spatial resolution, and point cloud registration [87]. The simple subtraction of two DEMs does not account for this DEM uncertainty, but several methods have been developed to account for it. A simple measure of precision can be used to determine a site-wide minimum level of detection, and elevation changes lower than this value are discarded [88]. However, this approach assumes a constant uncertainty across the whole area, not considering that the DEM uncertainty is inherently different across a heterogeneous landscape [89]. Despite the difficulty in quantifying it, a spatially variable measure of uncertainty is therefore desirable for heterogeneous surfaces [55]. Wheaton et al. [55] proposed a fuzzy inference system (FIS) to quantify the spatially varied uncertainty of DEMs and subsequent DoDs. A FIS has been implemented in the Geomorphic Change Detection software alongside several tools for estimating DoD uncertainty when outside estimates of error are provided [55]. However, the application of a FIS relies on established rules between input parameters, which may vary depending on survey methods and study sites. This makes it difficult to establish the rules without a priori knowledge of the factors affecting elevation uncertainty, and necessitates significant effort to calibrate and test the parameters [90]. Therefore, there is still no easy method for deriving DoDs with spatially varied uncertainty directly from dense point clouds.

In this paper, we present a straightforward method to produce DoDs from dense point clouds with spatially varied uncertainty. Based only on point cloud data, this method allows for implementing spatially varied uncertainty in DoD analysis when precision measures are unavailable. It uses the information inherent in the point cloud to estimate spatially varied uncertainty while retaining the DoD's ability to estimate volume changes. The method, named Las2DoD, is coded in Python with a standalone graphical user interface (GUI). It provides a fast and easy way to detect surface changes and quantify erosion and deposition, as well as the net volume changes of a surface. Through its simple implementation, this method may be advantageous over other methods where the proper input parameters are unclear or unavailable.

# Theory Background and Methodology

## *Error Propagation in DoD*

If only considering vertical uncertainty, the true elevation of a DEM cell, $Z_{Actual}$, can be represented as [55]:

$$Z_{Actual} = Z_{DEM} \pm \delta z \tag{1}$$

where $Z_{DEM}$ is the elevation of a DEM cell, and δz is the elevation uncertainty. Only vertical uncertainty is considered, as horizontal uncertainty, when it is much smaller than the DEM cell size, has little effect on vertical differences in low slope areas [55]. The value of *δz* can be estimated by different methods, including the standard error from independent check data [44,88,91], the interpolation of vertical standard deviations [43,78], and the root mean square error of data against known control points [59]. The errors inherent to each DEM propagate into the subsequent DoD [92]. The propagated error for the DoD, $\delta u_{DoD}$, can be estimated by [93]:

$$\delta u_{DoD} = \sqrt{(\delta z_{new})^2 + (\delta z_{old})^2} \tag{2}$$

where $\delta z_{new}$ and $\delta z_{old}$ represent the uncertainties of the DEMs at two times. This propagated error can be estimated by a minimum level of detection threshold applied to all DEM cells or by a spatially explicit level of detection with a spatial *δz* estimate. Assuming that *δz* can be estimated using the standard deviation of error of points within a DEM cell, a probabilistic threshold can be derived using a *t*-statistic of the two point datasets from the DEM cells at two times [94]:

$$t = \frac{\left|Z_{DEM_{new}} - Z_{DEM_{old}}\right|}{\delta u_{DoD}} \tag{3}$$

This *t*-test produces a *p*-value for each DEM cell, representing the probability of the derived *t* score on the *t*-distribution determined by its degrees of freedom. The propagated error, $\delta u_{DoD}$, can be estimated independently based on repeated measurements of the same set of control points, or based on the number of points measured from each cell, assuming the elevation variance of these points represents the uncertainty. In this study, we used the latter assumption because there are typically insufficient repeated measurements of control points to represent a heterogeneous landscape. In contrast, when point clouds are dense compared to the gridding resolution—as they are in TLS or SfM—the points within each grid cell provide sufficient information to estimate the propagated error.

Due to the potential difference in the numbers of points within each DEM cell at the two times, and considering that surfaces can influence the variability in erroneous points, it is highly likely that errors in DEMs used in surface change detection do not have an equal number of points and variance. Therefore, an unequal variance *t*-test is necessary to determine the confidence interval. The unequal variances *t*-test is also known as Welch's *t*-test [95]. Welch's *t*-test is given by:

$$t = \frac{\bar{X}_1 - \bar{X}_2}{\sqrt{\frac{s_1^2}{N_1} + \frac{s_2^2}{N_2}}} \tag{4}$$

where $\bar{X}_1$ and $\bar{X}_2$ are the mean point elevations, $s_1$ and $s_2$ are the standard deviations, and $N_1$ and $N_2$ are numbers of points from each cell of the two DEMs, respectively. The degrees of freedom ($df$) for the Welch's *t*-test is defined as:

$$df = \frac{\left(\frac{s_1^2}{N_1} + \frac{s_2^2}{N_2}\right)^2}{\left(\frac{s_1^4}{N_1^2(N_1 - 1)} + \frac{s_2^4}{N_2^2(N_2 - 1)}\right)} \tag{5}$$

***Las2DoD***

We developed an algorithm to conduct DoD analysis with spatial varied uncertainty directly based on dense point clouds at two times. Figure 1 illustrates the process flowchart. This algorithm first grids each point cloud based on the specified resolution. The point count (*N*), mean (*X*), and standard deviation (*s*) of the points in each cell are derived for each point cloud. Then, Welch's *t*-test is conducted as described above to calculate the *t*-score for each cell using Equation (4) and derive the *p*-value based on the *t*-distribution associated with its degrees of freedom. The *p*-value is used to

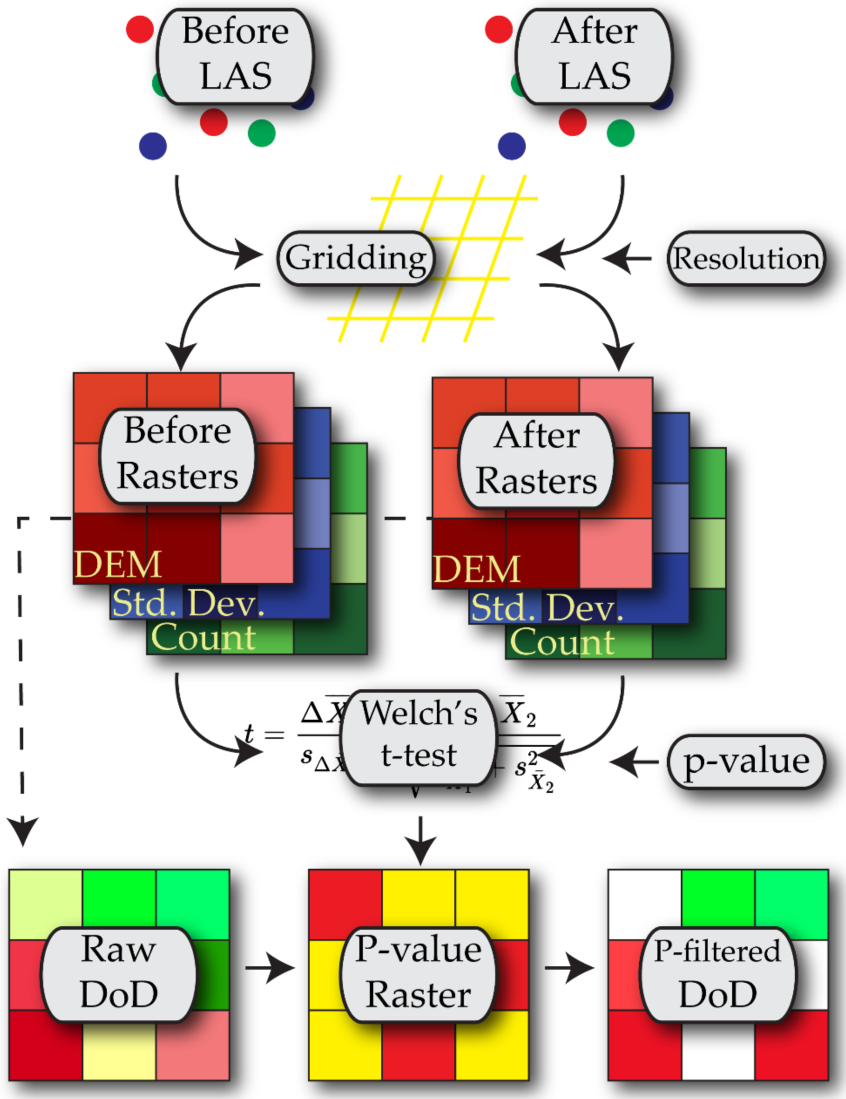


**Figure 1. Flowchart showing an overview of the Las2DoD process**

determine whether the cell elevation difference is statistically significant at a critical confidence level, such as an alpha level of 0.05 or 95% confidence interval. Finally, a filtered DoD raster is created to show the cells with statistically significant changes. For comparison, the algorithm also generates an unfiltered DoD raster without consideration of uncertainty, a *t*-score raster, and a *p*-value raster. The total area and volume changes in erosion and deposition, as well as the net volume change, are also summarized as a text (csv) file.

The above algorithm is coded in Python based on freely available scipy, gdal, and numpy libraries. A standalone user-friendly GUI was also developed to let users specify input point clouds, parameters, and an output folder (Figure 2). Before and after point clouds, a grid resolution, and a target *p*-value are all that are necessary for this tool to operate. The input point clouds must be in LAS format and are assumed to have approximately the same spatial extent. The X, Y, and Z units of the point clouds must be consistent, and the same units are used for the grid resolution. The input grid resolution is used to determine the grid size for grouping and processing points, as well as the row, column, and resolution of the final rasters. The target *p*-value will be used as a confidence interval—for example, the target *p*-value for the 95% confidence level is 0.05—to filter out insignificant results based on the cell-by-cell two-tailed Welch's *t*-test. The tool also offers an option to only conduct the DoD analysis to a specific area of interest (AOI) if a masking raster is provided. This masking raster should only contain data within the AOI and use the same unit and coordinate system as the input point clouds. This tool also derives an estimate of the mass of sediment added/removed if an optional soil bulk density is provided. If desired, this tool can also create detailed statistics for each point cloud as raster outputs, such as mean, standard deviation, and point count. The source codes and the executable file for Las2DoD can be found at 'https://github.com/GeneBailey/Las2DoD'.

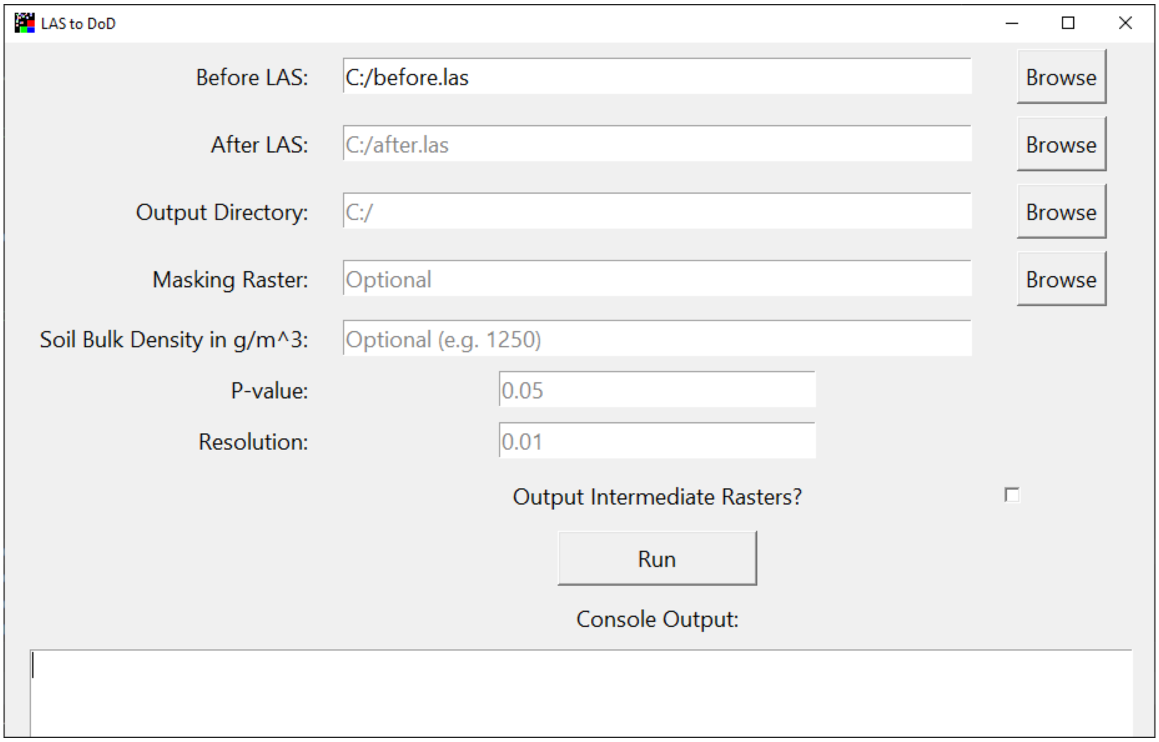


**Figure 2. Las2DoD GUI Interface**

# Case Study

We demonstrated the Las2DoD method on a case study to quantify fine-scale soil erosion on two field plots in the southeastern United States. The results were then compared to the DoD analysis with a minimum level of detection ($\mathrm{LoD_{Min}}$) and the results from the M3C2 algorithm. The $\mathrm{LoD_{Min}}$ and M3C2 methods were selected for comparison due to their frequent appearance in the literature and accessible implementation through available software. With the exception of a single estimate, these two methods are similar to Las2DoD in that they require minimal data preparation and no prior knowledge of elevation uncertainty and related factors.

### *Study Area and Datasets*

Our field site is located at the Plant Science unit of the East Tennessee Research and Education Center (ETREC), University of Tennessee (35.89°, −83.95°) (Figure 3 and Figure 4a). Data were gathered from two experimental plots on the field site. Each plot is approximately 70 m in length, 6 m in width, and on a 15% slope. The plots have been maintained largely free of vegetation through the application of herbicide and the burning of the remaining residue (Figure 3). The plots have different microtopographic features and are not considered replicates. Some rills have developed on the left plot (Plot A) in Figure 4a, especially the one deeply incised rill on the middle-left part (Figure 4b). No rills have developed on the right plot (Plot B), but this plot has some slight ridges running the length of the interior (Figure 4a). These two plots provide the opportunity to test the efficiency of the Las2DoD method to quantify both rill and sheet erosion.

Raised berms were constructed at the sides and top of the plots to control the surface flow. A flow divider system was installed at the bottom of each plot to capture runoff and sediment eroded from the plots (Figure 4b), as used in multiple erosion studies [96–99]. This flow divider system is designed to capture a precise fraction of up to 3000 gallons of runoff between samplings [100]. Six concrete mounting points were also installed at the corners of each plot as fixed locations for placing registration targets (Figure 4a).


(**a**)

(**b**)

**Figure 3. (a) Photograph of study site from the bottom of the slope. Plots A and B are indicated; (b) Close photo of Plot A soil surface**

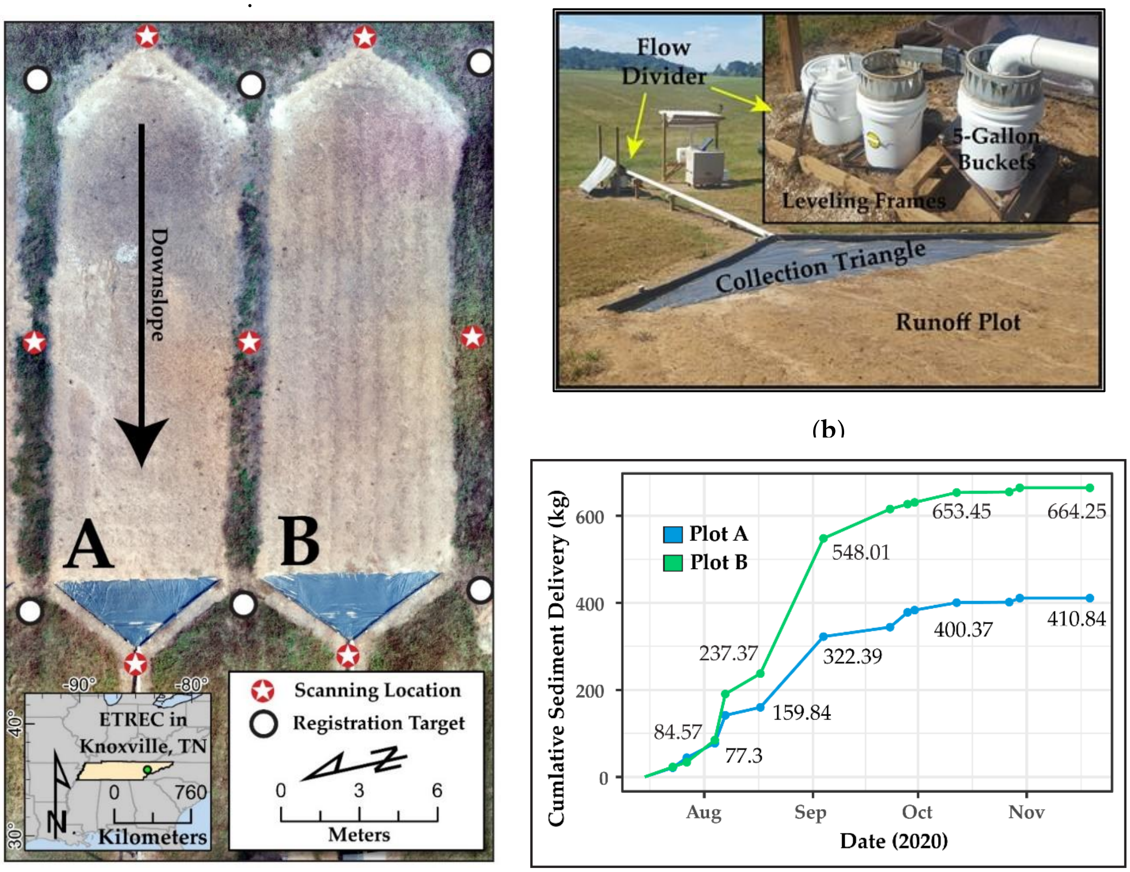


(b)

(a)

(c)

**Figure 4. (a) East Tennessee Research and Education Center (ETREC) study site with plots A and B used in the case study; (b) Photograph showing the flow divider system on plot B; (c) Cumulative sediment delivery data sampled from the field plots**

TLS scans were conducted on 6 July 2020 and 19 November 2020. At each date, seven scans were collected by putting the scanner at the top, bottom, and sides of each plot (Figure 4a). All scans were collected using a FARO Focus3D X 330 mounted on a leveled extending tripod. A scanning resolution of half the sensor's full capability was used to balance the point density and scanning time, producing more than 176 million points over the full field of view for each scan, with an average point spacing of 3 mm at a 10 m distance. The operating time of each scan was roughly 8 min. Using Leica Cyclone software, all TLS point clouds (seven from each date) were registered into a single local coordinate system based on the positions of spherical targets placed on the mounting points at the corners of the plots (Figure 4a). This achieved a positional mean absolute error of 3.5 mm for the final registration. The mean absolute error reported by the Leica Cyclone is defined as an average of the absolute positional distances in the x, y, and z axes between the targets before and after registration [101]. A unified point cloud was then exported for each plot at each scan date. While ground filtering is often a critical step to remove vegetation and other non-ground points when quantifying surface changes from TLS data [60], this study did not apply any ground filtering except for the removal of some noise points far from the plot surface because these well-maintained plots are largely free of vegetation. This practice allowed us to limit the potential smoothing effect of ground-filtering algorithms on surface change detection.

During the study period, sediment was sampled from the flow divider system whenever 2 inches of precipitation occurred at the nearby McGhee Tyson Airport weather station about 11 km away. We sampled the collected sediment 13 times during the study period. The cumulative sediment delivered for plots A and B were 411 kg and 664 kg, respectively (Figure 4c). To enable the estimation of soil mass lost/gained, the soil bulk density of the plots was measured using a nuclear gauge reading the backscatter of the top five centimeters of soil [102,103]. Plot A recorded an average bulk density of 1.25 $g/cm^{3,}$ and Plot B had an average bulk density of 1.39 $g/cm^3$. The volume of change estimations from DoDs can be converted to a net mass change based on these bulk densities. The net mass change estimated from the implemented surface change detection methods can then be compared to the total sediment collected from the flow divider system.

### *Change Detection Methods*

Three methods were used to quantify the topographic changes during the study period. The grid size for the analysis was 1 cm. Studies have suggested that the cell resolution used in the analysis does affect the quantification of surface changes [75]. In our study, a 1 cm resolution provides enough point data within each cell to conduct statistically meaningful analysis while being fine enough not to overgeneralize surface changes. The 1 cm cell size is also much larger than the registered error of point clouds (3.5 mm), limiting the effect of horizontal uncertainty on the DoD analysis [55].

As described in Section 2, Las2DoD requires the input of two point clouds, a target *p*-value, a cell resolution, and a masking raster. Here, we used the July and November point clouds for each plot, a 0.05 *p*-value, a cell size of 0.01 m, and a masking raster representing the interior of each plot. The output was compared to the output of the $\mathrm{LoD_{Min}}$ and M3C2 methods.

We used the Geomorphic Change Detection software developed by Wheaton et al. [55] to implement the $\mathrm{LoD_{Min}}$ method. DEMs for each plot were generated from point clouds from the July and November scans based on the average elevation falling within each 1 cm cell. The DEMs were clipped to only cover the extent of the interior bounds of each plot. In the GCD software, a DoD analysis was performed for each plot using the July and November DEMs and a minimum level of detection threshold of 3.5 mm, corresponding to the point cloud registration error derived from the targets. The resulting DoDs only account for the changes in the cells where the estimated surface change is more than 3.5 mm.

We also used the M3C2 plugin in the open-source CloudCompare software (http://cloudcompare.org/, accessed on 20 March 2022) to conduct point cloud-based change detection analysis. The guidance for this tool suggests that the normal scale parameter is set to a value that is about 25 times the estimated surface roughness at that scale, and the projection scale parameter is large enough that the generated cylinder encompasses on average 20 points while still being small enough to not over-average the distances [52]. For these plots, the values of 0.025 m and 0.01 m for the normals scale and projection scale, respectively, were found to satisfy the recommendations. The normals were calculated using the default settings and operating on every point within the July point clouds. The max depth or height of the cylinder used to identify distance points was set to 2 m to sufficiently include any points. The registration error of 3.5 mm was also included in the uncertainty estimate. The M3C2 generates a point cloud with 'M3C2 Distance', 'Significant Change', and 'Distance Uncertainty' data fields. The points where the distance calculation was not considered significant were filtered from further analysis. M3C2′s distancing estimation operates exclusively on points with various normal directions, and it is hard to directly convert them to volume changes. To enable a comparison to DoD results, the M3C2 output was gridded into 1 cm cells by assigning each cell's value with the average M3C2 distance of points within the cell. In this way, the M3C2 output can be transformed into a raster format to allow for the calculation of volume changes [36].

## Results

Tables 1 and 2 list the performance of each method relative to the plot measurements from plots A and B, respectively. For Plot A, among these three methods, Las2DoD estimated 369 kg of mass lost, about 90% of the total 411 kg measured sediment at the bottom of the plot. In comparison, $\mathrm{LoD_{Min}}$ and M3C2 estimated 70% and 58% of the total measured sediment, respectively. In comparison, the accuracy of all methods was decreased for Plot B, although a similar pattern exists among the three methods. Las2DoD generated the most accurate estimate and captured 63% of the measured sediment delivery of 664 kg, whereas the $\mathrm{LoD_{Min}}$ and M3C2 methods only estimated 48% and 30% of the measured sediment delivery, respectively. In terms of the number of cells with statistically significant changes, the three methods were substantially different.

**Table 1. Results from applying the three change detection methods in comparison with the plot measurements for Plot A.**

| Method | Area of Significant Change (m2) | Percentage of Surface Represented (%) | Volume Added (m3) | Volume Removed (m3) | Total Volume Change (m3) | Estimated Mass Change (kg)[1] | Estimated Mass Change / Measured Sediment Delivery[2] |
|---|---|---|---|---|---|---|---|
| Las2DoD | 101.65 | 79.5 | 0.05 | 0.34 | -0.30 | -369 | 0.90 |
| M3C2 | 16.48 | 12.9 | 0.01 | 0.2 | -0.19 | -237 | 0.58 |
| $LoD_{Min}$ | 39.74 | 31.1 | 0.02 | 0.25 | -0.23 | -287.5 | 0.70 |

[1]Estimated Mass Change is equal to the Total Volume Change multiplied by the plot's soil bulk density of 1.25 g/cm3. [2]The Measured Sediment Delivery of Plot A is 411 kg.

**Table 2. Results from applying the three change detection methods in comparison with the plot measurements for Plot B.**

| Method | Area of Significant Change (m2) | Percentage of Surface Represented (%) | Volume Added (m3) | Volume Removed (m3) | Total Volume Change (m3) | Estimated Mass Change (kg)[1] | Estimated Mass Change / Measured Sediment Delivery[2] |
|---|---|---|---|---|---|---|---|
| Las2DoD | 112.36 | 83.7 | 0.06 | 0.36 | -0.30 | -416 | 0.63 |
| M3C2 | 14.68 | 10.9 | 0.02 | 0.16 | -0.14 | -198 | 0.30 |
| $LoD_{Min}$ | 46.07 | 34.3 | 0.03 | 0.26 | -0.23 | -320 | 0.48 |

[1]Estimated Mass Change is equal to the Total Volume Change multiplied by the plot's soil bulk density of 1.39 g/cm3. [2]The Measured Sediment Delivery of Plot B is 664 kg.

Las2DoD identified 79.5% (Plot A) and 83.7% (Plot B) of the total plot areas to have significant changes, while M3C2 identified only 12.9% and 10.9% and $\mathrm{LoD_{Min}}$ 31.1% and 46.07% for these two plots, respectively. For both plots, the methods that reported a greater percentage of cells with significant change also estimated the net mass change more accurately.

Figures 5 and 6 illustrate the spatial distribution of the detectable changes captured by each method alongside a Raw DoD created by simply subtracting DEMs without any consideration of uncertainty. The Raw DoD is included to provide spatial context for the DoD cells excluded through uncertainty testing, but it is not used as a measure of performance. All methods capture the areas of the most extreme change, as can be seen by the areas of deposition at the tops and edges of both plots and the large erosional feature at the middle-left of Plot A. Unsurprisingly, the areas with minimal distance differences are excluded by all methods. In agreement with Tables 1 and 2, Las2DoD captures more cells of change than the other methods, and a large portion of the captured cells are of lower magnitude changes. In cells where both Las2DoD and $\mathrm{LoD_{Min}}$ detect significant changes, the values of the changes are identical. This is not necessarily true for M3C2 because M3C2 calculates distances between the surfaces along the normal direction, whereas Las2DoD and $\mathrm{LoD_{Min}}$ strictly measure the vertical distance. This is evidenced by several areas along the right side of Plot A and the top of Plot B, which are identified as strongly erosional in the M3C2 results but are largely absent in other DoDs.

Figure 7 shows the histograms of the DoD results for each plot, highlighting the changes discarded by different methods. The histograms for both plots appear remarkably similar. Without the consideration of uncertainty, the raw DoDs appear to both have a normal distribution around a mean change of $-2.3$ mm and $-2.2$ mm for plots A and B. Las2DoD detects less change around zero relative to the raw DoD but still retains some surface changes within $\pm$ 3.5 mm that are discarded when using the $\mathrm{LoD_{Min}}$ and M3C2 methods.

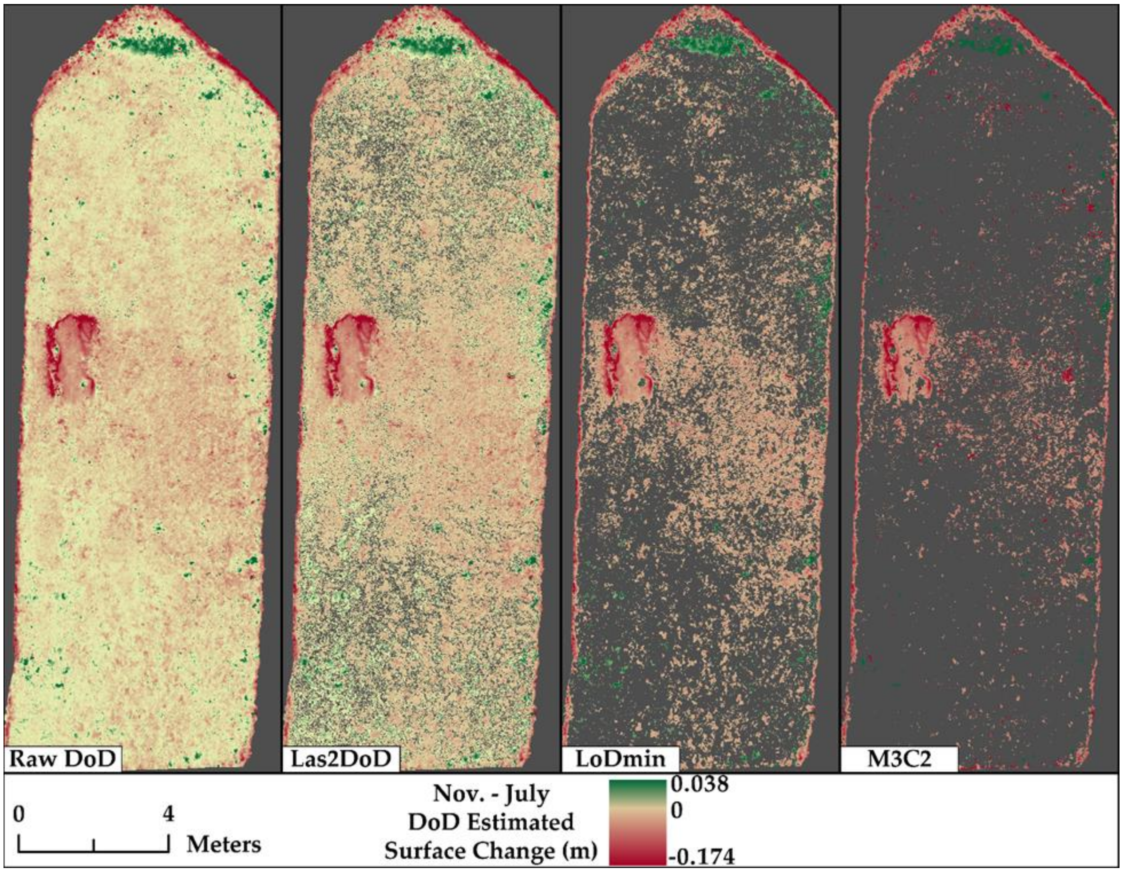


**Figure 5. DoD results from Plot A of a DoD without uncertainty analysis and the three tested methods with uncertainty testing.**

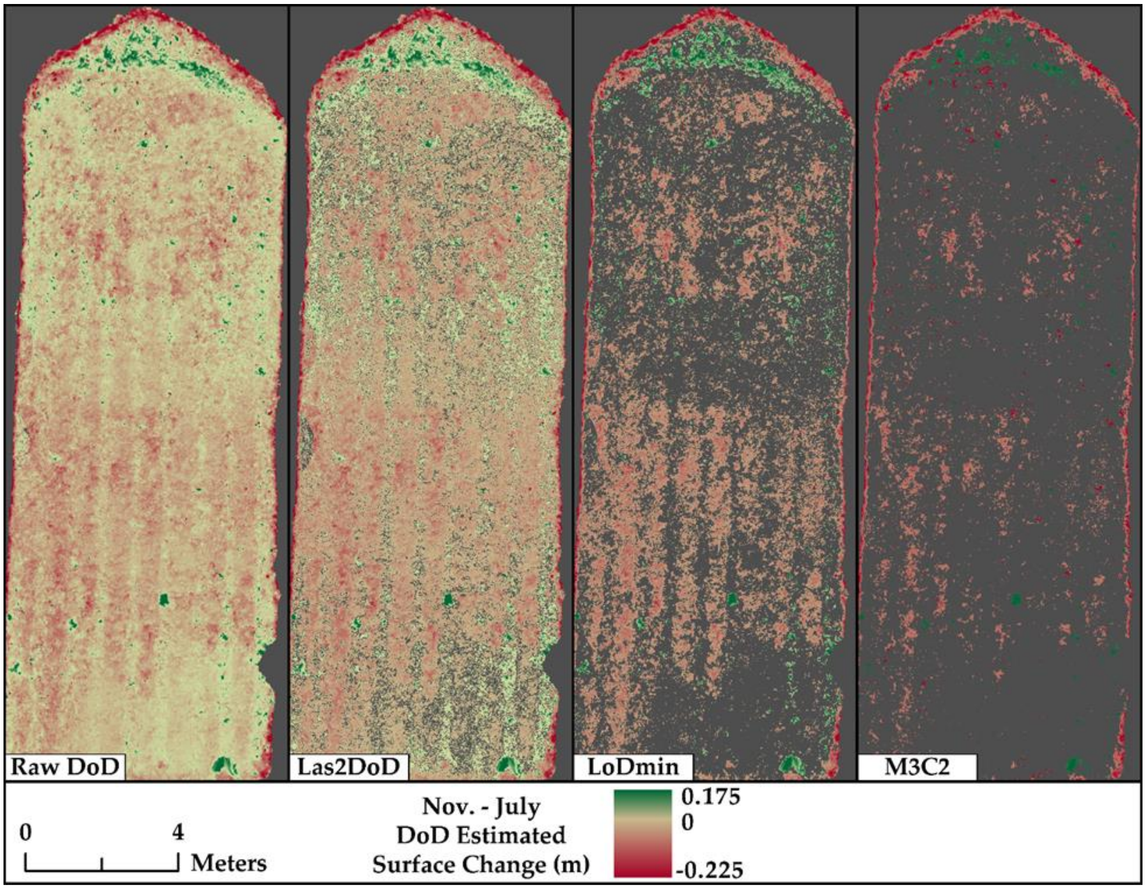


**Figure 6. DoD results from Plot B of a DoD without uncertainty analysis and the three tested methods with uncertainty testing.**

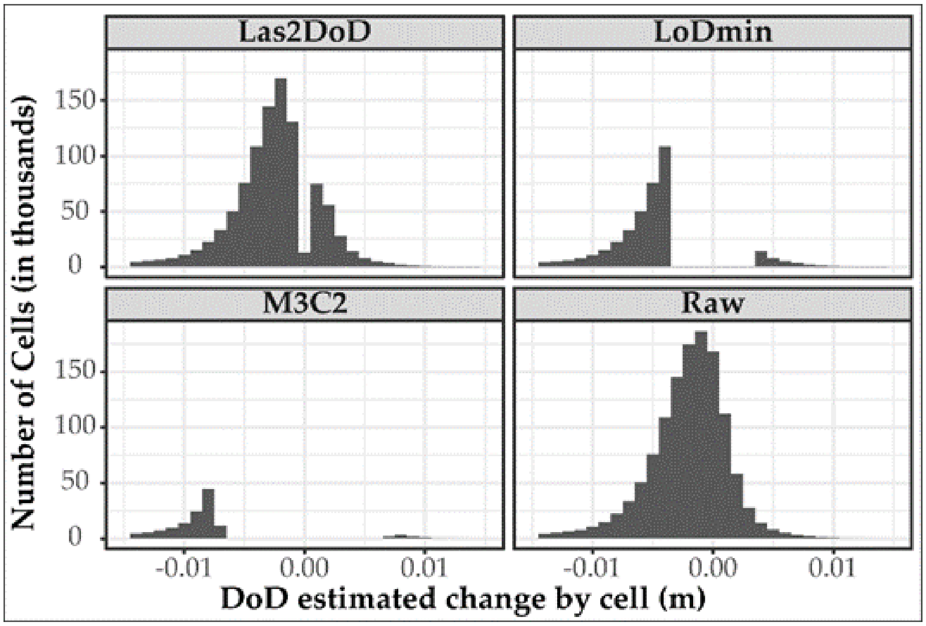


(**a**)

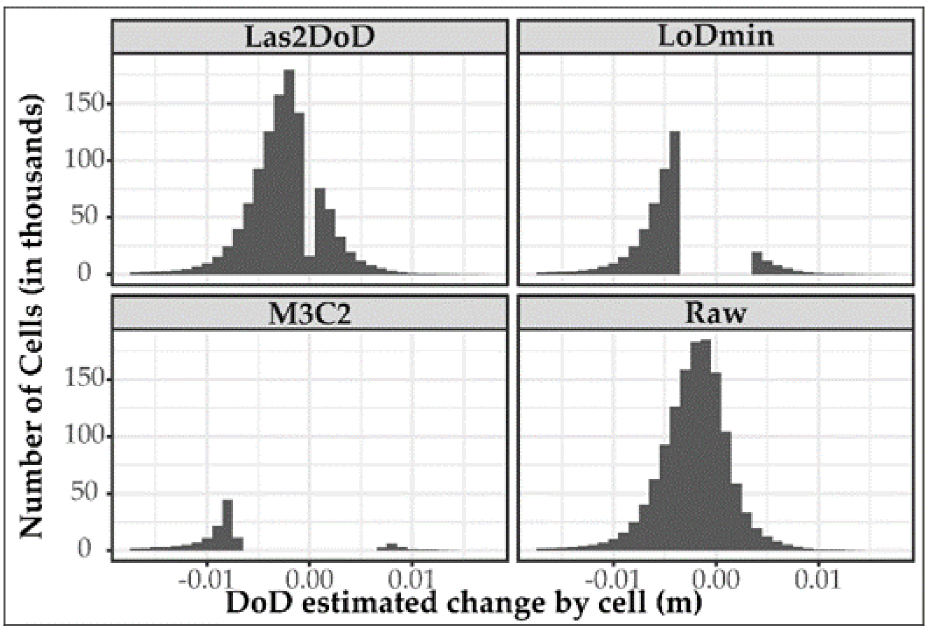


(**b**)

**Figure 7. Histograms from the final DoD of the selected uncertainty analysis methods and a raw DoD without uncertainty analysis for Plot A (a) and Plot B (b)**

## Discussion

Compared to the measured plot sediment delivery, Las2DoD produces the most accurate estimates of sediment mass delivery at 90% and 63% for plots A and B, respectively. The performative difference between plots A and B relative to the measured sediment delivery is attributed to the prevalence of sheet erosion on Plot B, which is inherently more challenging to capture. Las2DoD also discerns a greater surface area of change, representing 75% and 83% of the total surface area. This result suggests that Las2DoD can be used in situations where surface change is spread out spatially, but the magnitude of change is at a scale similar to the positional uncertainty of the derived surfaces, as is often the case in areas experiencing interrill erosion. The interrill areas have been found to contribute to as much as 46% of the total erosion on a bare tilled plot with developed rills [27]. It is therefore essential for Las2DoD or other similar methods to account for spatially varied uncertainty and discern minor surface changes in order to capture a total picture of hillslope erosion.

Note that the Las2DoD method ignores registration errors or any errors incorporated into the point cloud before using the method. In performing Welch's *t*-test, Las2DoD's uncertainty analysis can reduce the effect of outliers and noisy points given enough correctly placed points within a cell. When these erroneous points increase the vertical standard deviation of a cell surface such that the difference of means cannot discern a statistically significant difference, the cell will be disregarded. This is not true for methods only considering distance differences, like $\mathrm{LoD}_{\mathrm{Min}}$, where if the outlier-affected distance is greater than the threshold, it will be included in the analysis.

The uncertainty analysis will not handle systematic errors within a point cloud, like tilting resulting from an improper registration. While $\mathrm{LoD}_{\mathrm{Min}}$ and M3C2 are likely over-conservative in accounting for registration errors, obscuring minor surface changes, Las2DoD may capture more erroneous change due to registration error. The registration error observed for this case study (3.5 mm) is based on the deviation of points recorded on registration targets at the corners outside of the area of interest. This error is likely overestimated for most locations in the interior of the plot, as the propagated registration error from targets will increase with increasing distance between individual targets and the barycenter of all targets [101,104]. Although it is not directly accounted for within the Las2DoD method, care must be taken to ensure that the registration of point clouds is as accurate as possible to reduce the impact of systematic errors.

While Las2DoD estimated 90% of the measured sediment delivery for Plot A, it is not an indication that this method always produces this level of accuracy, as highlighted by Plot B. The absolute accuracy results are likely site-specific and related to a combination of local topography, registration, the absence of large vegetation, scan point density, and cell resolution. Accurately measuring small-scale diffuse erosion is a complex task, but the performance of Las2DoD relative to the other studied methods suggests that Las2DoD may positively contribute to the accuracy of DoD estimations. For this case study, Las2DoD includes more cells of minor change to derive more accurate results than the other two methods, which are more conservative due to the inclusion of likely overestimated registration error. The difference between the results of these methods may be reduced on surfaces that experience extreme changes, such as gully erosion and streambank erosion.

Las2DoD only requires a grid resolution and *p*-value as parameters, both of which can be easily conceptualized and determined. This presents a potential advantage over other, more complex methods like M3C2. While more robust to the influences of local topography, the selection of the suitable parameters for M3C2 can be especially difficult when lacking empirical data to assess the performance of the algorithm under different parameter settings. Therefore, Las2DoD provides an easy and fast way to detect surface changes, and it can be beneficial over other methods where the proper input parameters are unclear or unavailable. In addition, Las2DoD can also generate a set of intermediate rasters, such as the mean and standard deviation rasters of the point cloud, which can be integrated with the Geomorphic Change Detection software or many other terrain analysis software packages for additional analyses.

Las2DoD operates best when the combination of point density and selected grid resolution allow for a high number of points within each cell because it relies on cell-by-cell statistical analysis. The current version of Las2DoD assigns the elevation of each DEM cell as the mean height of the points with the cell to be consistent with Welch's *t*-test. The minimum point elevation is occasionally used to inform DEM elevation [42,47]. Many studies also assign an interpolated elevation value using nearest neighbor interpolation [78], bilinear interpolation [75], a triangulated irregular network [44], inverse distance weighting [47], or kriging [57]. Future work is needed to explore the alternate cell height assignments in the Las2DoD analysis. At the same time, the spatial resolution of the specified grid also affects the representation of the surface. Although it is generally believed that finer resolutions provide more precise representations of the surface, finer resolutions also make the final DEM more sensitive to outliers and potentially create more cells with no data [75]. Therefore, more work is necessary to determine the optimal cell resolution for DoD analysis.

While Las2DoD is intended to be used broadly, it is important to note that the case study in this paper represents highly controlled conditions using TLS and its related processing workflow. The controlled nature of the case study limits confounding factors and offers a promising basis to build upon. Further investigation is needed before Las2DoD is recommended to be applied to natural conditions. Future studies may investigate the application of Las2DoD using other sources of high-density points clouds like SfM, explore the performance of the method on different terrains under a variety of conditions, or assess the impact of alternative registration and filtering approaches.

## Conclusions

This paper presents a straightforward method—Las2DoD—to generate DoDs from point clouds with spatially varied uncertainty. This method uses a specified cell size to derive the mean and standard deviation of the elevations of the points, as well as the point count within each cell of the point clouds collected at different times. These derived datasets are then applied in a Welch's *t*-test to test whether each cell has a significant difference in mean elevation based on a specified confidence level. The results from the *t*-test are used to filter cells with insignificant changes. The whole process is coded in Python with a standalone GUI.

This proposed method was applied to a case study using TLS point clouds to quantify mixed rill–interrill erosion on natural rainfall hillslope erosion plots and compared the results with the results estimated by a minimum level of detection filtered DoD and a DoD summarized from the M3C2 algorithm. The results of these methods are also compared with the measured sediment delivery from the plots to assess the performance of each method. Our results indicate Las2DoD has the best performance with an estimation of 90% of the measured sediment on the plot with rill erosion, whereas the other two methods estimated 70% and 58% of the total measured sediment, respectively. For the plot dominated by sheet erosion, the absolute accuracy of all methods was reduced, but the performance pattern between the methods was highly similar. Both plots demonstrate that Las2DoD captures more low-magnitude topographic change, while the other methods are more conservative and only capture relatively high-magnitude changes.

Las2DoD offers a simple and straightforward way to implement DoD analysis with spatial varied uncertainty. It provides a fast and easy way to detect surface changes and quantify erosion and deposition, as well as the net volume changes of a surface. This method only requires the dense point clouds and easily conceptualized and determined cell size and confidence level, without additional information or extensive parameterization. It may be particularly useful when other DoD methods may be over-conservative, and the change experienced on a large portion of the surface is of low magnitude but may contribute to a significant portion to change in elevation, such as the interrill erosion of hillslopes.

# CHAPTER II

# COMPARISON OF GROUND POINT FILTERING ALGORITHMS FOR FINE SPATIAL RESOLUTION EROSION STUDIES USING TERRESTRIAL LIDAR

## Abstract

Multitemporal Terrestrial LiDAR (Light Detection and Ranging) can monitor erosion by detecting topographic change using 3D point clouds. Because even centimeter-level decreases in a surface can represent an unsustainable amount of erosion, it is critical to detect the soil surface at fine spatial scales where the interpretation of the surface is susceptible to non-soil points. Due to the large amount of data created by fine resolution LiDAR scans, it is vital to filter non-soil points in a reproducible manner. Point cloud filtering algorithms classify a 3D point cloud into ground and off-terrain (OT) points and have potential use in fine resolution LiDAR studies. This paper explores the performance of three filtering algorithms, a cloth simulation filter, a modified slope-based filter, and a random forest classifier, in identifying OT points. We scanned a hillslope plot before and after removing vegetation from the plot. These two scans generated a test dataset of ground and OT points based on a Cloud-to-Cloud (C2C) comparison. Each filtering algorithm was then tested against the training dataset with various input parameter/model sets to obtain the highest performance. The cloth simulation filter produced the best classification with a kappa value of 0.86, but the 'time step' parameter highly influences the performance. The modified slope-based filter had the highest precision of ground classification at 0.94, although only scoring a 0.62 kappa value. The random forest classifier produced balanced classification results with a kappa value of 0.75 based on 15 features. This work provides valuable insight into the use of filtering algorithms to classify fine spatial resolution Terrestrial LiDAR datasets.

## Introduction

Light detection and ranging (LiDAR) technologies are capable of producing highly precise three-dimensional (3D) topographic data by emitting lasers and measuring their return time [40]. It has the capability to estimate erosion without the surface disturbance and labor required to capture and measure eroded sediment in the field. When operated from aircraft, LiDAR sensors can measure 3D data on scales from a single kilometer to more than a hundred kilometers [72–74]. LiDAR sensors are widely employed on the ground to acquire a significantly higher measurement density when the objects being measured are much smaller in spatial extent. A high density and fine spatial resolution are necessary to estimate soil erosion. In particular, when erosion is dispersed across space as sheet or interrill erosion, an unsustainable level of erosion can result from millimeter-scale surface changes. Ground-based LiDAR operated from tripods is known as Terrestrial Laser Scanning (TLS). TLS has been used in various settings where accurately measuring surface changes necessitates high point density and precision, such as hillslopes [47,75,76], tilled soils [79–81], badlands [49], erosion plots [78], gullies [41–44,48], bluffs [51], and channels [57].

When measuring surface changes from point clouds at fine spatiotemporal scales where TLS is frequently used, special care needs to be taken to mitigate the effect of erroneous non-ground points [47,75]. Non-ground or off-terrain (OT) points can have many sources like scanner error, noise, vegetation, or ground litter. Any point obscuring the accurate representation of the ground surface reduces the accuracy of subsequent analysis. Therefore, most uses of TLS data are accompanied by a point cloud filtering process to isolate ground points. Filtering can substantially increase the accuracy of a point cloud represented surface at fine resolutions [60,61].

Many approaches have been used in filtering point clouds. TLS point clouds can be manually examined to remove non-ground points [36,39]. Although it is a straightforward approach, manually filtering points can be labor-intensive, and the results are not easily replicated. Automatic filtering approaches that are repeatable with minimal user input are beneficial when the data quantity is relatively high, particularly in multitemporal TLS datasets [64]. Several automatic filtering algorithms have been developed and deployed in TLS land change studies, such as the inverted cloth simulation filter (CSF) [65], a modified slope-based filter (MSBF) [66], and a random forest (RF) classifier filter [105]. Subsequent research is needed to choose and implement an automatic filtering algorithm for a given surface. The performance assessment of several filtering algorithms against a series of manually classified TLS datasets found that no single algorithm is sufficient for all surfaces of the dataset [71].

This study explores the performance of three filtering algorithms: CSF, MSBF, and RF, in identifying ground points from a high-density fine-scale TLS dataset. Successive TLS scans, one scan under highly vegetated conditions and a second under bare conditions, were collected from a controlled erosion plot and processed to produce an empirically derived testing dataset. This testing dataset was used to tune the algorithm parameters and measure the performance of each filtering algorithm. The following questions are addressed using these results: Can any of the filtering algorithms effectively remove the vegetation points at fine resolutions? Which set of parameters for each algorithm accomplishes the best performance? This study provides critical insight into the ground point filtering process, which is essential in using TLS to quantify fine-scale surface changes.

## Study Area

The study area is an experimental field site located at the Plant Science unit of the East Tennessee Research and Education Center, University of Tennessee (ETREC) (Figure 8). Data were collected from a hillslope plot at the site. The plot has an approximate length of 21 m, a width of 6 m, and a slope of 15%. The plot is designed to be hydrologically isolated from the greater hillslope, with raised berms at the top and sides of the plot and a sediment capturing installation at the bottom. The plot was used for a subsequent study that required it to be bare, so it was established to be largely free of vegetation with the application of herbicide, allowing time for vegetation to die off and burning off all remaining residues. Photographs demonstrating this process can be seen in Figure 9. The plots underwent no physical disturbance during these processes nor for the 10 prior years, so the soil surface elevation should not have been measurably affected. The establishment process presents a chance to capture the same plot under different vegetation conditions within about a month.

Because consistent control points are critical to LiDAR data, permanent concrete mounting piers were installed at the corners of the plot to serve as locations for

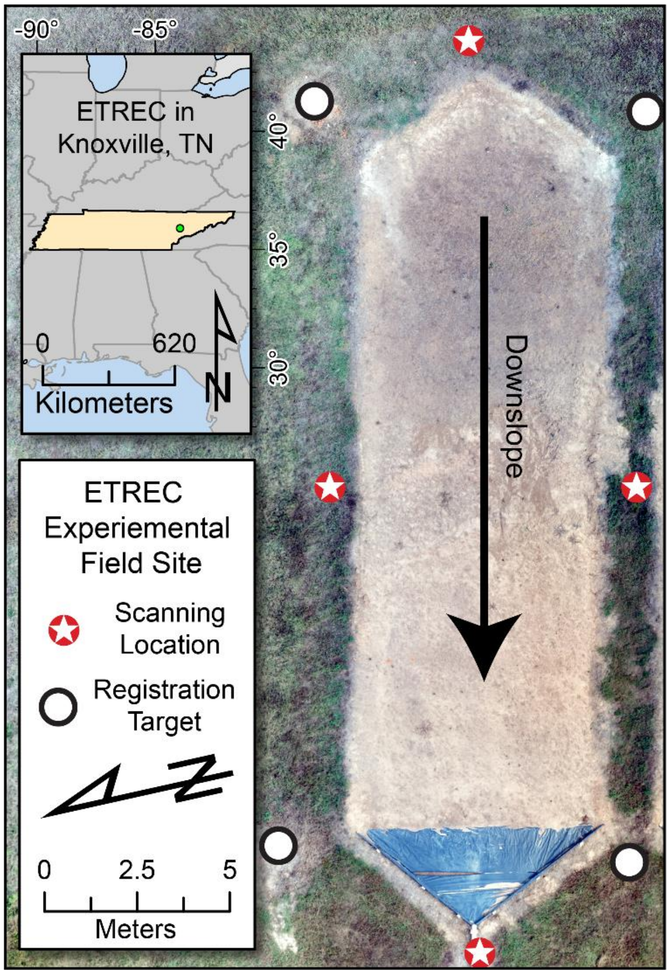


**Figure 8. East Tennessee Research and Education Center (ETRC) study site**


**Figure 9. Vegetation removal process**

registration targets. Considering the strength of TLS in delineating 3D shapes, identical spherical registration targets with a diameter of 139 mm were used.

## Methods

### *Research Design and Filtering Algorithms*

Figure 10 shows a flowchart of the whole research design. A test dataset of classified point clouds is needed to assess the performance of different filtering algorithms and the impact of filtering parameters. Several studies have classified points by hand for this purpose, but manually classifying points is time-consuming and labor-intensive [62,71,105]. In this study, successive TLS scans were collected from the studied plot. One scan was conducted under highly vegetated conditions, and the second scan was conducted under bare conditions after removing vegetation. These two scans are processed to produce the testing dataset to tune the algorithm parameters and measure the performance of each filtering algorithm.

Three automated filtering algorithms, CSF, MSBF, and RF, were selected and applied to the testing dataset. These algorithms were selected because they are freely available, can be implemented programmatically, and operate only on the positional information of the point cloud (X, Y, Z).

The CSF algorithm is a surface-based classifier designed for airborne LiDAR that can be conceptualized as a cloth falling over an inverted point cloud. Places touching or within a threshold of this cloth are classified as ground, and the remaining points are classified as OT points. The CSF filter has been implemented in python and MATLAB and is included with the CloudCompare software as a plugin. For this study, CSF is applied through python Anaconda binaries.

The MSBF is a conventional morphology and slope-based technique which uses a white top-hat transformation to equalize ground elevation differences between points before analyzing the slope and height between a point and its neighbors. Points exceeding a set height and slope threshold within a neighborhood are classified as OT points and the

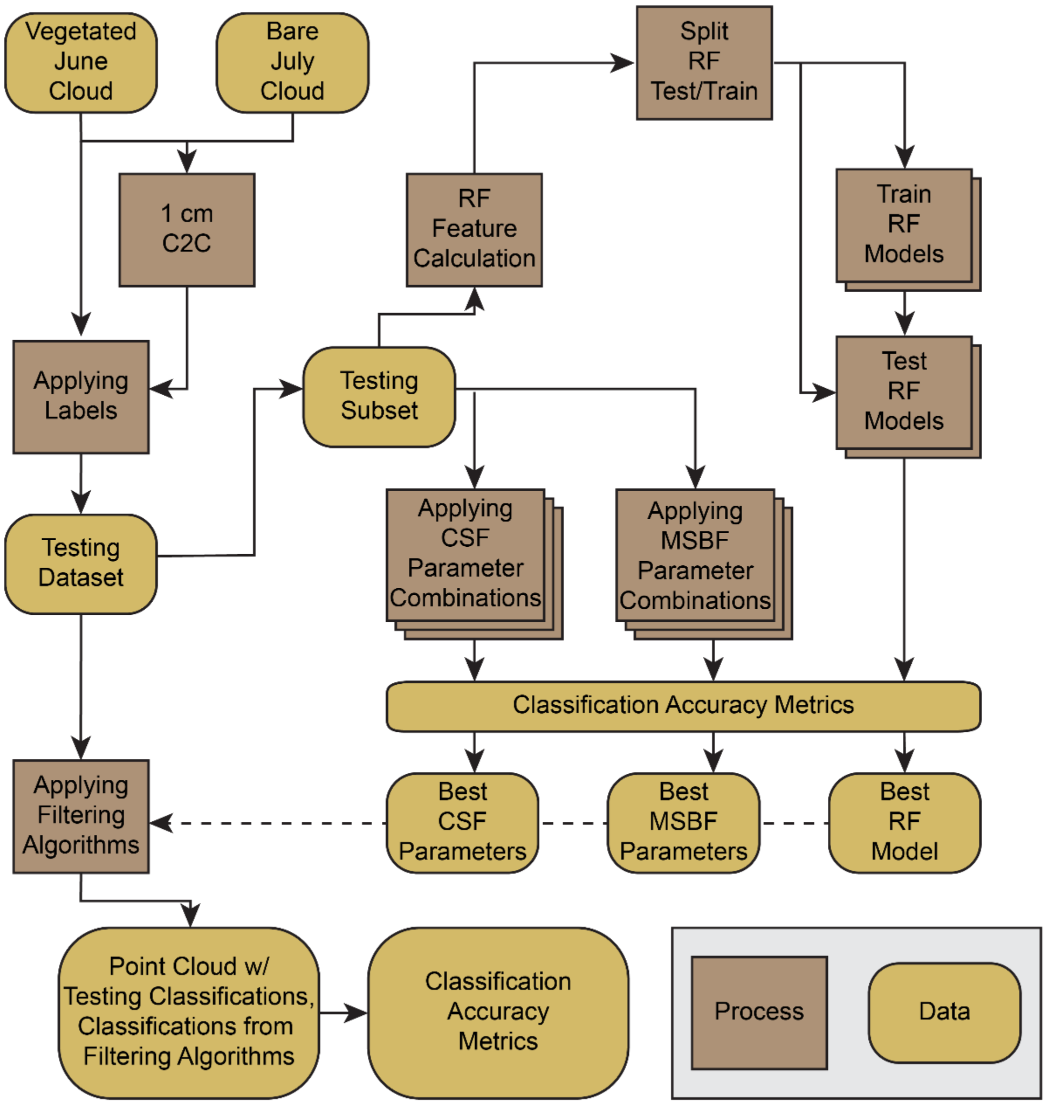


**Figure 10. Flowchart of the research design**

remaining points as ground. Adjustable parameters for the MSBF algorithm are ‘radius’, ‘minimum neighbors’, ‘slope threshold’, ‘height threshold’, and ‘slope normalization’. This algorithm is available through WhiteBoxTools with command-line tools, a python library, and software implementations [106]. The python implementation is used in this study.

A Random Forest Classifier is a supervised machine learning algorithm that classifies points based on a ‘forest’ of decision trees built automatically from relationships between identified features in training data. The RF classifier can be tuned with hyperparameters. Similar to Weidner et al. [105], this study deviates from default settings by using 100 trees with a maximum tree depth of 1000. RF training data is composed of features that are used to predict labels. The OT points classified in the testing dataset make up the labels for this study. The features used to predict the labels are the three normalized eigenvalues calculated at each point, considering all points within a neighborhood radius of 0.5 cm, 0.75 cm, 1 cm, 1.5 cm, and 2.5 cm, similar to Weidner et al. [105]. This results in five features for each neighborhood, for a total of fifteen features considering five spatial scales. The eigenvalues were normalized by dividing a given eigenvalue by the sum of all three eigenvalues for the considered neighborhood radius. Two models were built and tested on a subset of the testing dataset. The first model considered the full range of neighborhood eigenvalues, and the other model only the 0.5 cm, 1 cm, and 1.5 cm neighborhood eigenvalues. Conceptually, this should allow the classifier to consider the shape of the surface at slightly different scales. Eigenvalues were calculated using CloudCompare command-line tools. The points within a subset of the testing dataset were randomly split 75/25% for training and testing purposes when building and comparing the two models. The RF classifier was implemented using the sklearn python library [107].

While the CSF and MSBF methods require input parameters, this implementation of the RF algorithm builds a model requiring defined features from testing data to set internal parameters. To examine the influence of different sets of parameters for CSF and MSBF, several hundred combinations of a range of parameters were applied to a subset of the testing dataset encompassing the central portions of the plot (Figure 11). The same subset was also used as training data to build the RF models. The subset of the testing dataset contains approximately 7 million total points, with 2.8 million points classified as ground and 4.2 million points classified as OT. A subset of the testing dataset was used for analyzing parameters and building the RF model because the subset was found to give reasonably close results to the entire dataset while significantly speeding up computation time when exploring parameters.

### ***Data Collection, Registration, and Preprocessing***

Two TLS surveys were conducted on 6/4/2020 (June scan) and 7/6/2020 (July scan). The June scan captured plot conditions before removing vegetation and contains dense live and dead, standing and flat vegetation on the plot. The July scan was conducted under bare plot conditions after vegetation was almost completely removed through herbicide and burning. All scans were collected using a FARO Focus3D X 330. This scanner has a laser wavelength of 1550 nm, a beam divergence of 0.19 mrad, and a beam diameter at exit of 2.25mm. The scanner is rated to measure the distance to surfaces from 0.6 m – to 130 m with a ranging error of ± 2 mm at 20 m. The device's field of view is 360° horizontal and 300° vertical. The scanner is mounted on an extending tripod to gain a favorable scanning angle. After an approximate alignment of the tripod, the scanner's internal dual-axis compensator levels the scan data with an accuracy of 0.015°. A scanning resolution of 0.5 of the scanner's full capability is used to balance the density of points with scan time, which results in over 177 million points over the entire field of view with an average point spacing of 3 mm at a 10 m distance and a scan time of roughly 8 minutes. Scans were collected with the scanner at the top, bottom, and sides of the plot to gain a more even distribution of point densities and a greater likelihood of points reaching the ground (Figure 8). Each scan renders a point cloud file that reports each point with geometric fields (X, Y, Z), color fields (R, G, B), and return intensity.

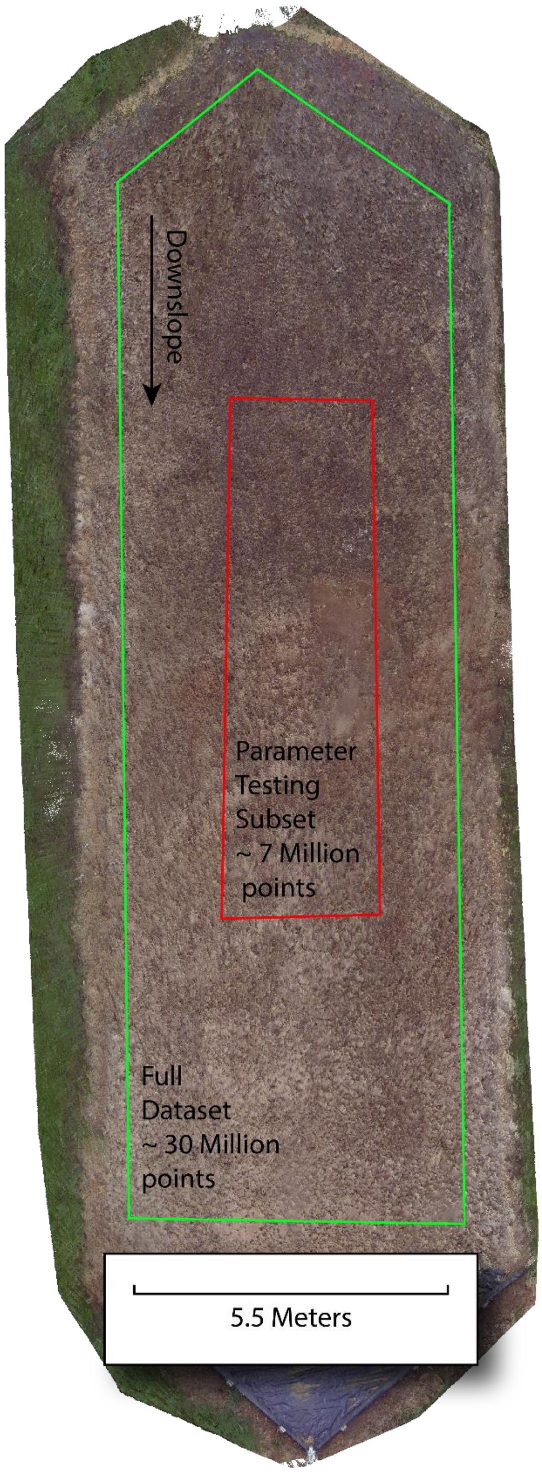


**Figure 11. Full testing dataset and subset of the testing dataset used to analyze parameters and models**

Raw TLS scans were registered using Leica Cyclone software. After importing, the spherical registration targets were manually identified. All eight scans were registered into a single local coordinate system using only the identified spherical registration targets. The resulting registration reported a positional mean absolute error, the average absolute movement in the X, Y, and Z axes of all registration targets during registration, of 3.5 mm. Individual viewpoint scans for the plot at each date were then merged and exported for a total of two point clouds. These clouds are manually clipped to include only points within a boundary about a half meter away from the plot edge to reduce the size of the data before further processing, as seen in Figure 11

Assuming that the June and July scans truly measured the same surface with and without vegetation, any point within the vegetated June point cloud whose distance away from the nearest point in the bare July cloud is greater than the registration error could be reasonably classified as an OT point. However, removing vegetation from the plot took around a month, and the plot did experience natural rainfall during this time. The weather station at the McGhee Tyson Airport, 9.5 km away, recorded 98.2 mm of precipitation between the June and July scan. While the vegetation and residue were still present on the plot providing some protection until just before the July scan, it can be assumed that the plot did experience some degree of natural erosion. To account for this, the threshold distance between points in the June and July clouds used to classify a point as OT was set to 1 cm after visual inspection. Any point in the vegetated June point cloud at least 1 cm away from the nearest point in the bare July point cloud was classified as an OT point. This distance is considered sufficiently far that the great majority of points in the June cloud that are at least 1 cm away from the July cloud and thereby classified as OT are a result of genuinely representing a non-ground object rather than a result of noise or an eroded surface. The distances between point clouds were calculated using the cloud-to-cloud (C2C) distance tool within the CloudCompare software, which computes an unsigned distance between every point in one cloud and the nearest point in another cloud. After running the C2C tool on the June and July scans, a binary field was generated for the vegetated June point cloud identifying each point as ground or OT if the

C2C distance was less than or greater than 1 cm, respectively. This classification field is treated as a truth label for further analysis of the performance of the filtering algorithms

### *Performance Assessment Methods*

The results were analyzed using a set of classification accuracy metrics, including overall accuracy, F1-score, recall, and precision. Excluding overall accuracy, the accuracy metrics are defined in the following equations using the terms of a binary classification confusion matrix: true positive ($TP$), true negative ($TN$), false positive ($FP$), and false negative ($FN$). Precision, $P$, is defined as the ratio of correct positive classifications to all positive classifications (Equation 6).

$$P = \frac{TP}{TP + FP} \tag{6}$$

Recall, R, is defined as the ratio of correct positive classifications to all true positives (Equation 7).

$$R = \frac{TP}{TP + FN} \tag{7}$$

The F1-score, $F_1$, is the harmonic mean of precision and recall (Equation 8).

$$F_1 = 2 \times \frac{P \times R}{P + R} \tag{8}$$

F1-score, recall, and precision are reported for both OT and ground classes. Additionally, Cohen's Kappa score, $k$, was calculated and used as the primary metric for analyzing parameter performance and overall model performance (Equation 9).

$$k = \frac{2 \times (TP \times TN - FN \times FP)}{(TP + FP) \times (FP + TN) + (TP + FN) \times (FN + TN)} \tag{8}$$

Cohen's Kappa considers the possibility of agreement occurring by chance among raters [108] and is more robust to imbalances in the dataset. Unlike F1-score, recall, and precision, it provides a single agreement value that considers both classes. McHugh [109] suggests Cohen's Kappa scores above 0.6 indicate a 'Moderate' agreement, scores above 0.8 a 'Strong' agreement, and scores above 0.9 an 'almost perfect' agreement.

Considering the immense size of the dataset and the challenges of displaying three-dimensional data, the results for this study are spatially visualized using three smaller sites within the plot representing a range of conditions. At each site, the point cloud is viewed from two perspectives. A top-down perspective compresses the Z (height) axis, highlighting the X (side-to-side) and Y (up-and-down slope) axes. A side view looking upslope compresses the Y axis, showing the X and Z axes. At each site and from each perspective, the colors of the points in the point cloud are used to visualize site conditions, testing data, and algorithm results. The testing dataset classifications and RGB points from the bare and vegetated scans provide context for the surface. The results from each algorithm are shown using four classes. 'True Ground' and 'True OT' are points correctly classified as ground or OT. 'False OT' is a ground point in the testing dataset that the algorithm classified as OT, and 'False Ground' is an OT point in the testing dataset classified as ground by the algorithm. Using the same four classes, the results are also shown in a cross-sectional profile across the middle of the plot.

## Results and Discussion

### *Testing Dataset*

The testing dataset was created using the C2C distance in CloudCompare. Of the over 30 million points, approximately 13 million points had an absolute distance of under 1 cm between the June and July scans, and 17 million points had an absolute distance of over 1 cm. These points are classified as ground and OT, respectively. Figure 12 shows the histogram of the distribution of the distances and classifications. Cross sections of the testing dataset overlaying the bare June point cloud reveal a close agreement between the ground classified points and the points from the bare scan where vegetation is sparse (Figure 13). In highly vegetated areas, fewer points fall under the 1 cm threshold, and ground-classified points occur much more infrequently. Despite the 1 cm distance threshold between scans, there are points within the testing dataset that are misclassified as OT points. These misclassified points are true ground surfaces that experienced erosion between scans. An example of this error in the testing dataset can be seen in Figure 14 and the second cross section from the bottom at the 4 m length mark of Figure 13. The location containing this error is further discussed when observing its impact on

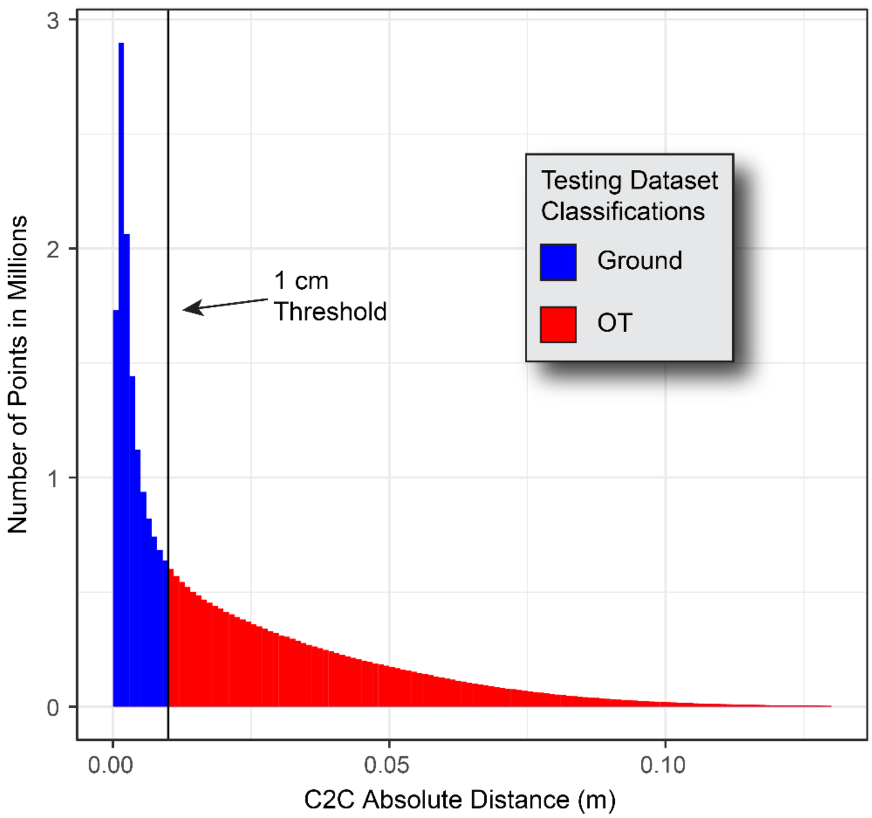


**Figure 12. Histogram showing the C2C absolute distances between the vegetated June scan and bare July scan.**

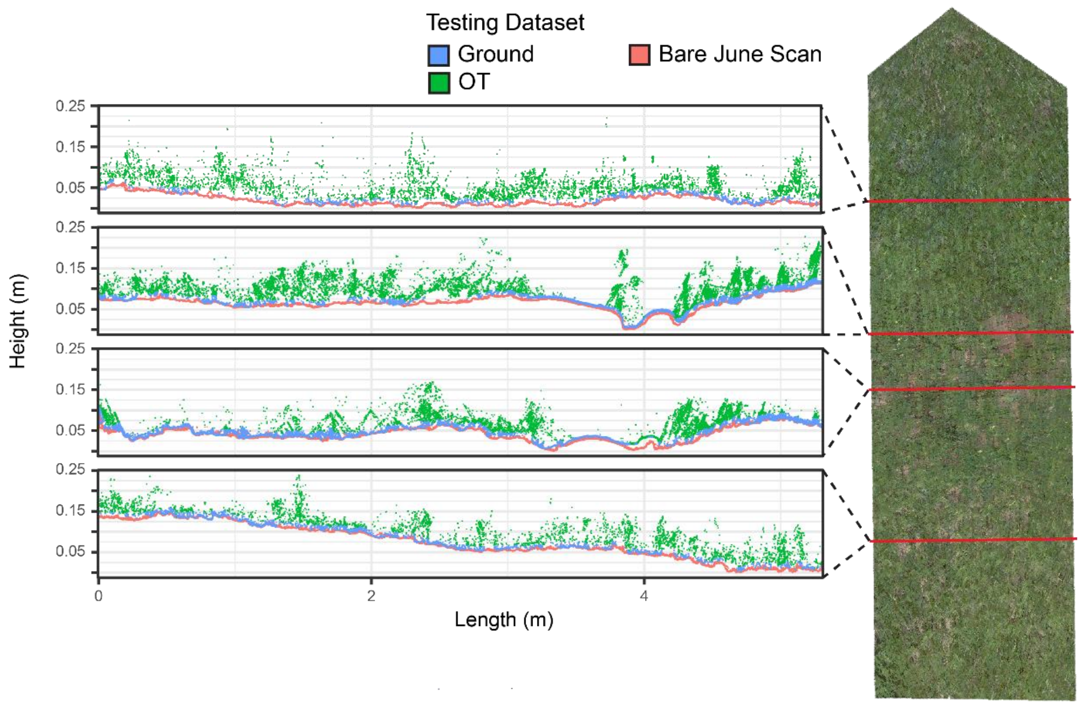


**Figure 13. Plot cross sections showing classified testing dataset points and bare June scan points**

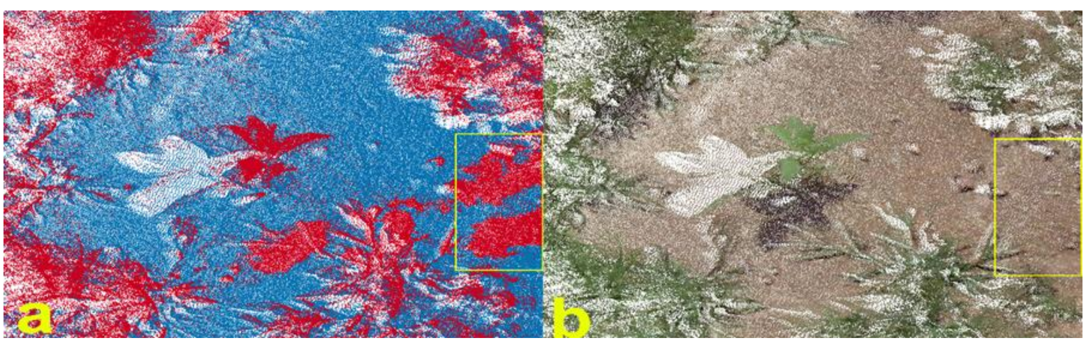


**Figure 14. (a) Testing dataset with OT classifications in red and ground classifications in blue. (b) Colored testing dataset subset. The yellow box highlights an area where erosive surface changes are incorrectly identified as OT points.**

filtering algorithms. In all observed data, this misclassification appears rare and is considered an acceptable trade-off to enable the automatic classification of over 30 million points.

### *Impact of Filtering Parameters on Performance*

The adjustable parameters of the CSF algorithm are 'smoothing', 'cloth resolution', 'rigidness', 'time step', 'classification threshold', and 'iterations'. Of these parameters, only 'cloth resolution', 'time step', and 'classification threshold' were found to substantially affect the classification of the testing dataset. The parameters that did not affect classification were set to the recommended default values of 'false', '3', 500' for 'smoothing', 'rigidness', and 'iterations', respectively. For the parameters found to affect classification, combinations of the following value ranges were used: 'cloth resolution' (from 0.002 to 0.012); 'time step' (from 0.1 to 0.65); 'classification threshold' (from 0.005 to 1). This resulted in 277 combinations of parameters being applied to a subset of the testing dataset. These values were selected considering the point density of the dataset and the expected scale of changes.

For the MSBF algorithm, combinations of input parameters of the following value ranges were used: 'radius' (from 0.005 to 0.07); 'minimum neighbors' (from 10 to 75); 'slope threshold' (from 40 to 54); 'height threshold' (from 0.005 to 0.02); 'slope normalization' (True, False). Seven hundred twenty-one combinations were applied to a subset of the testing dataset. As with the CSF, considering point density and surface topography, these values were selected as reasonable inputs.

Nearly 1000 iterations of input parameters for the CSF, MSBF algorithms, and two variations of RF models are applied to the interior subset of the testing dataset. The highest performing CSF parameter iteration resulted in a Kappa value of 0.87, with the lowest iteration resulting in a Kappa score of 0.24. Iterations of the CSF parameters where the 'time step' parameter was below 0.15 m resulted in a failed classification and disqualified from further analysis use. Of the impactful CSF parameters, the 'time step' parameter was most strongly correlated with the kappa score and appears to be the primary driver of algorithm performance (Figure 15). This result directly contrasts with a study testing the approach for airborne LiDAR, which found a CSF ‘time step’ parameter of 0.65 to apply to most situations [65]. The 0.65 default value produced the least accurate results for this dataset, with the smallest ‘time step’ values achieving the highest kappa score. This is likely a result of CSF being developed for airborne LiDAR, as the ‘time step’ controls the displacement of cloth particles, and the distances between ground and OT for TLS and airborne LiDAR are of a dramatically different scale. Our results suggest that the CSF filtering algorithm can produce excellent classifications on dense TLS datasets if the input parameters are carefully considered, as the parameter selection recommendations do not seem to apply to all point clouds. The sets of input parameters that produced the highest kappa value are given in (Table 3) and are further applied to the entire dataset.

The parameter iterations of the MSBF algorithm applied to the testing dataset subset produced a tighter range of kappa values from 0.67 to 0.52 than did CSF. For this dataset, the ‘Slope Threshold’ parameter had the closest correlation with algorithm performance (Figure 16). By simply observing the correlation of individual parameters with kappa, the individual impact of parameters is somewhat obfuscated by the interactions between parameters. Future research is needed for a more detailed sensitivity analysis on the impact of the MSBF parameters. In this study, the parameters producing the highest kappa value are listed in Table 3, and these parameters were applied to the entire testing dataset.

The performances of the two RF models were compared for the testing subset using a randomly generated 25% and 75% of points for model testing and training, respectively. The RF model built considering the eigenvalues of five neighborhood scales outperformed the model built on three scales in all metrics. The inclusion of two additional neighborhood scales, 0.75 cm and 2.5 cm, into the model’s base training dataset of 0.5 cm, 1 cm, and 1.5 cm increased the resulting kappa value from 0.63 to 0.72. Unsurprisingly, the inclusion of additional scales improved the classification results, although there will be a trade-off between the benefit of additional scales and increasing

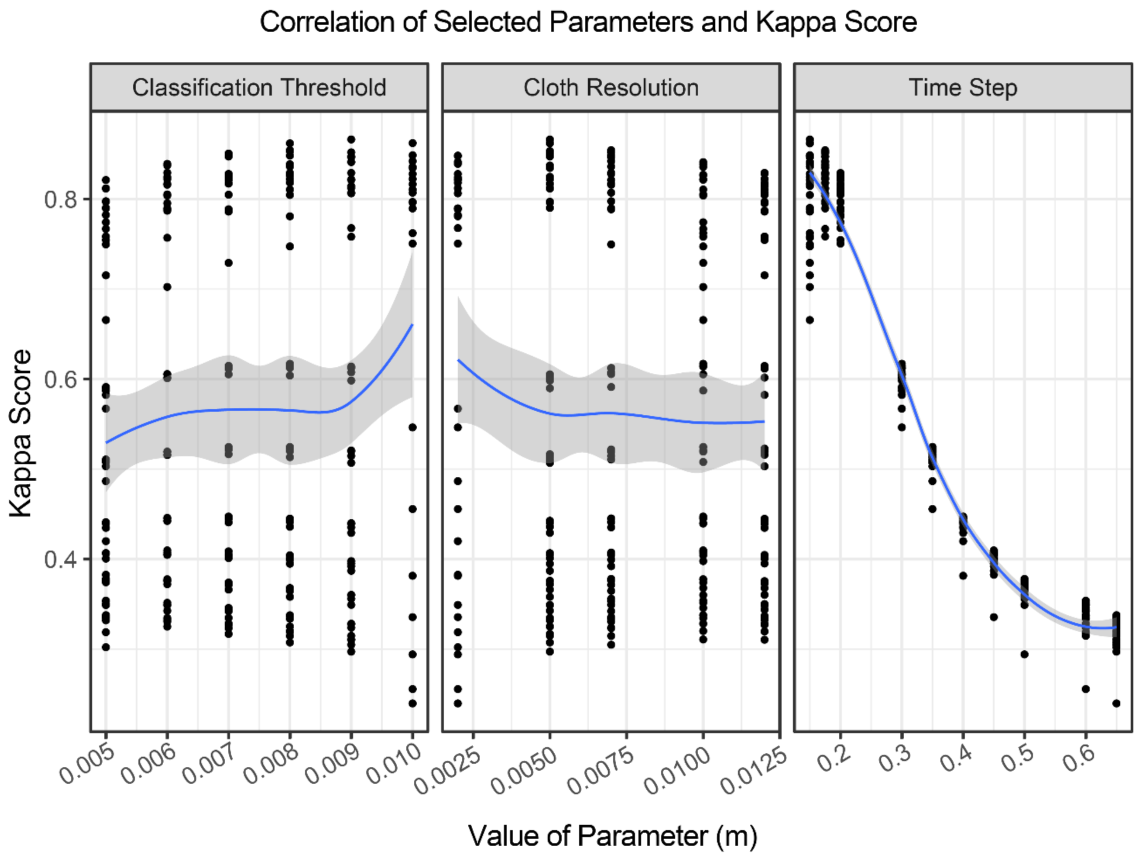


**Figure 15. CSF algorithm parameter performance results by Kappa score**

**Table 3. Highest performing input parameters for CSF, MSBF by Kappa score relative to the subset of the testing dataset**

| Filtering Method | Input Parameters | Best Value | Tested Range |
|---|---|---|---|
| **CSF** | | | |
| | Cloth Resolution | 0.005 m | 0.002 to 0.012 |
| | Time Step | 0.15 m | 0.1 to 0.65 |
| | Classification Threshold | 0.009 m | 0.005 to 1 |
| **MSBF** | | | |
| | Radius | 0.03 m | 0.005 to 0.07 |
| | Slope Threshold | 54 ° | 40 to 54 |
| | Height Threshold | 0.01 m | 0.005 to 0.02 |
| | Slope Normalization | TRUE | TRUE, FALSE |

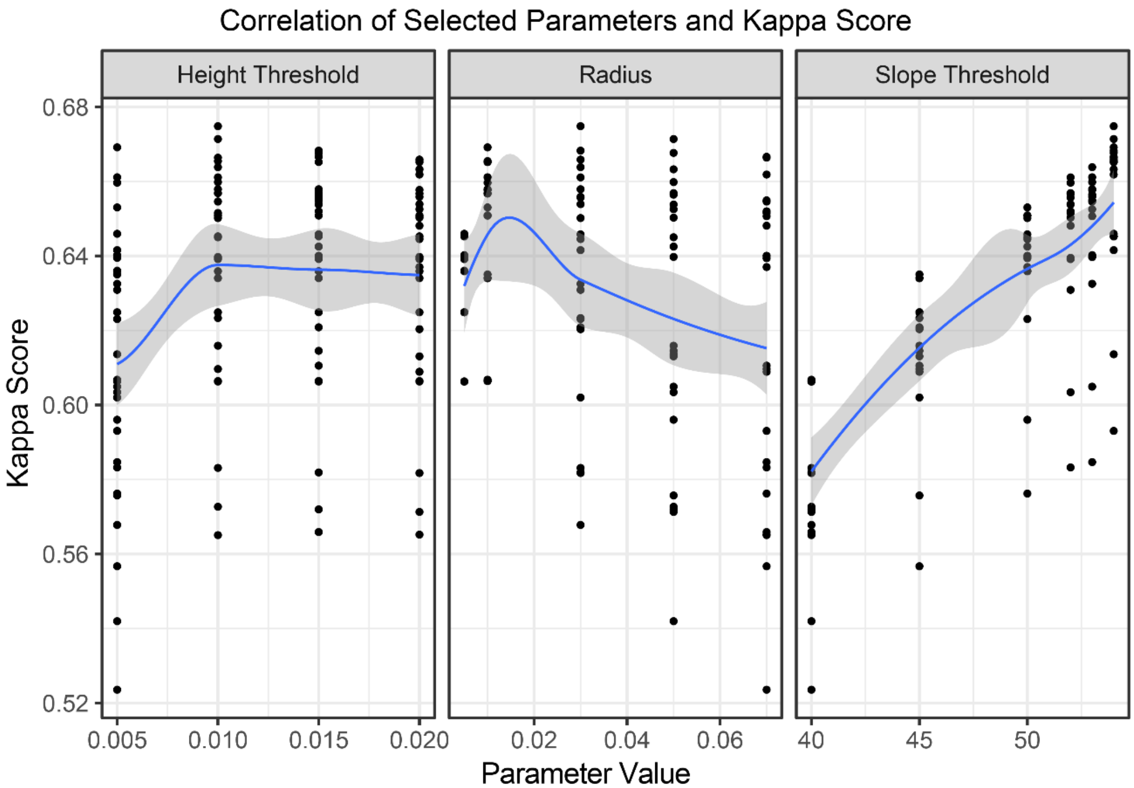


**Figure 16. MSBF algorithm parameter performance results by Kappa score**

computation time and complexity. For this dataset, improving the kappa value of the classification by 0.09 appears to be well worth the computational cost of moving from 3 neighborhood scales (9 features) to 5 neighborhood scales (15 features). The RF model built using the full range of neighborhood scales was then applied to the entire dataset to compare against the CSF and MSBF algorithms.

### *Comparison of Filtering Algorithms*

Only the optimal parameters/models were used for the whole testing dataset to evaluate the performances of CSF, MSBF, and RF approaches (Table 4). The CSF algorithm outperforms the other algorithms in most metrics except ground precision and OT recall, for which MSBF narrowly outperformed CSF. The accuracy metrics for CSF and RF are balanced between the ground and OT classes, with CSF scoring slightly higher in every category.

Figure 17 shows a portion of the plot free of vegetation. At this site, the few OT points of the testing dataset result from noise reflections and portions of a small pebble that moved into the area between scans. All algorithms easily identify these OT points. The only noticeable difference is with the MSBF, which consistently falsely classifies OT points over most of the surface. On closer observation, it is apparent that these falsely classified OT points prevalent in the MSBF results have positions that are slightly above the other ground points in flat areas. This positional pattern of points and their density suggests that they may originate from an individual scanning viewpoint farther away from the site. Because these points are classified as ground in the testing dataset and therefore are not more than a centimeter from the bare surface, MSBF likely classifies these points as OT because they are above the set slope threshold relative to the other points in the area. The cross section results also show this pattern for MSBF (Figure 18). All along the correctly classified ground points, there is a layer of falsely classified OT points that is not present in the other algorithms.

Figure 19 shows a portion of the plot dominated by plant cover. At this site, CSF is remarkably accurate relative to the other algorithms. CSF falsely classifies some OT

**Table 4. Accuracy metrics for all filtering methods on the full testing dataset. The highest performing algorithm in each metric is bolded.**

| Filtering Method | Overall Accuracy | Ground F1 | Ground Recall | Ground Precision | OT F1 | OT Recall | OT Precision | Cohen's Kappa |
|---|---|---|---|---|---|---|---|---|
| CSF | **0.93** | **0.92** | **0.95** | 0.90 | **0.94** | 0.92 | **0.96** | **0.86** |
| MSBF | 0.82 | 0.75 | 0.62 | **0.94** | 0.86 | **0.97** | 0.78 | 0.62 |
| RF | 0.88 | 0.88 | 0.87 | 0.88 | 0.88 | 0.88 | 0.87 | 0.75 |

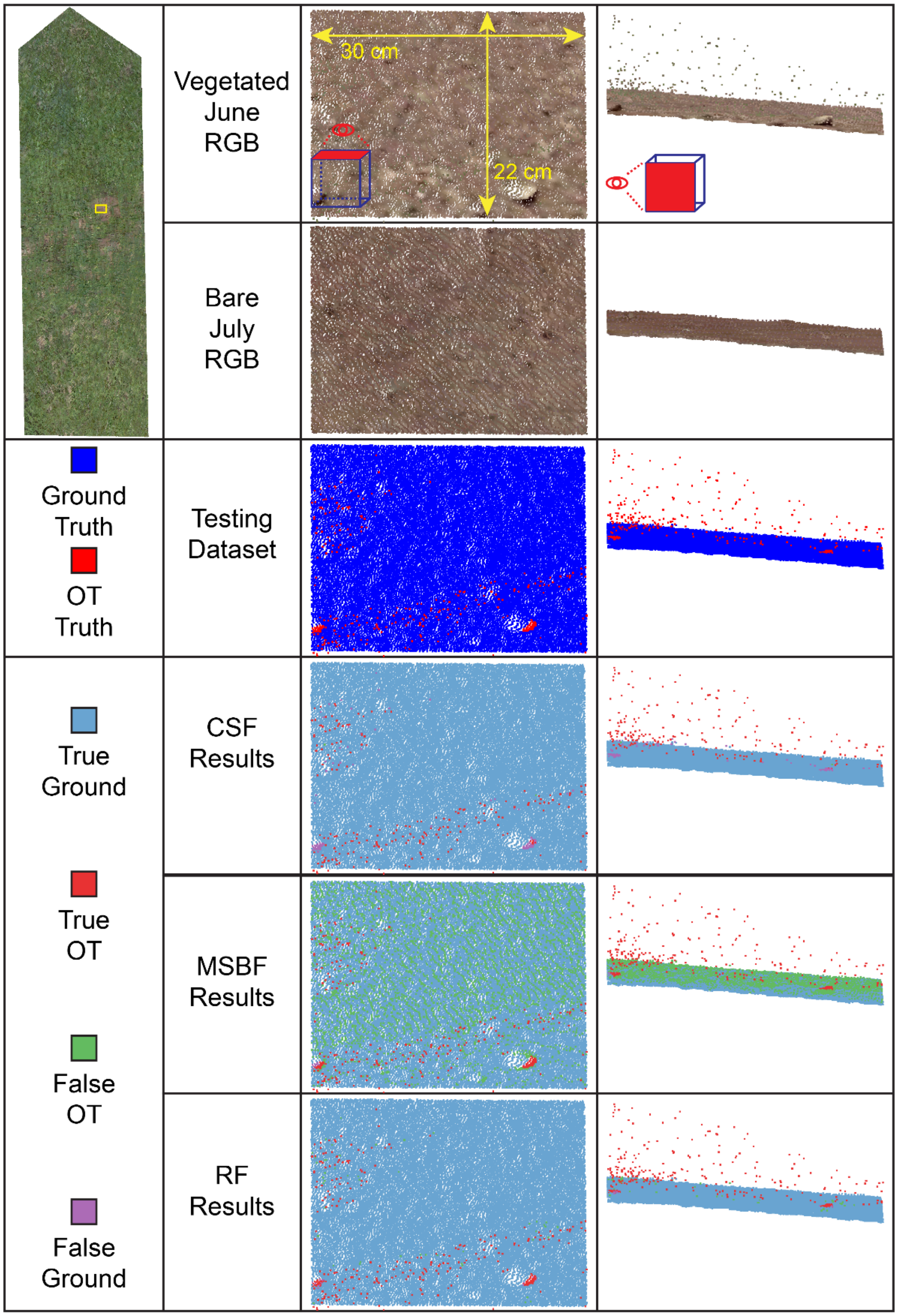


**Figure 17. Filtering results on a bare portion of the plot**

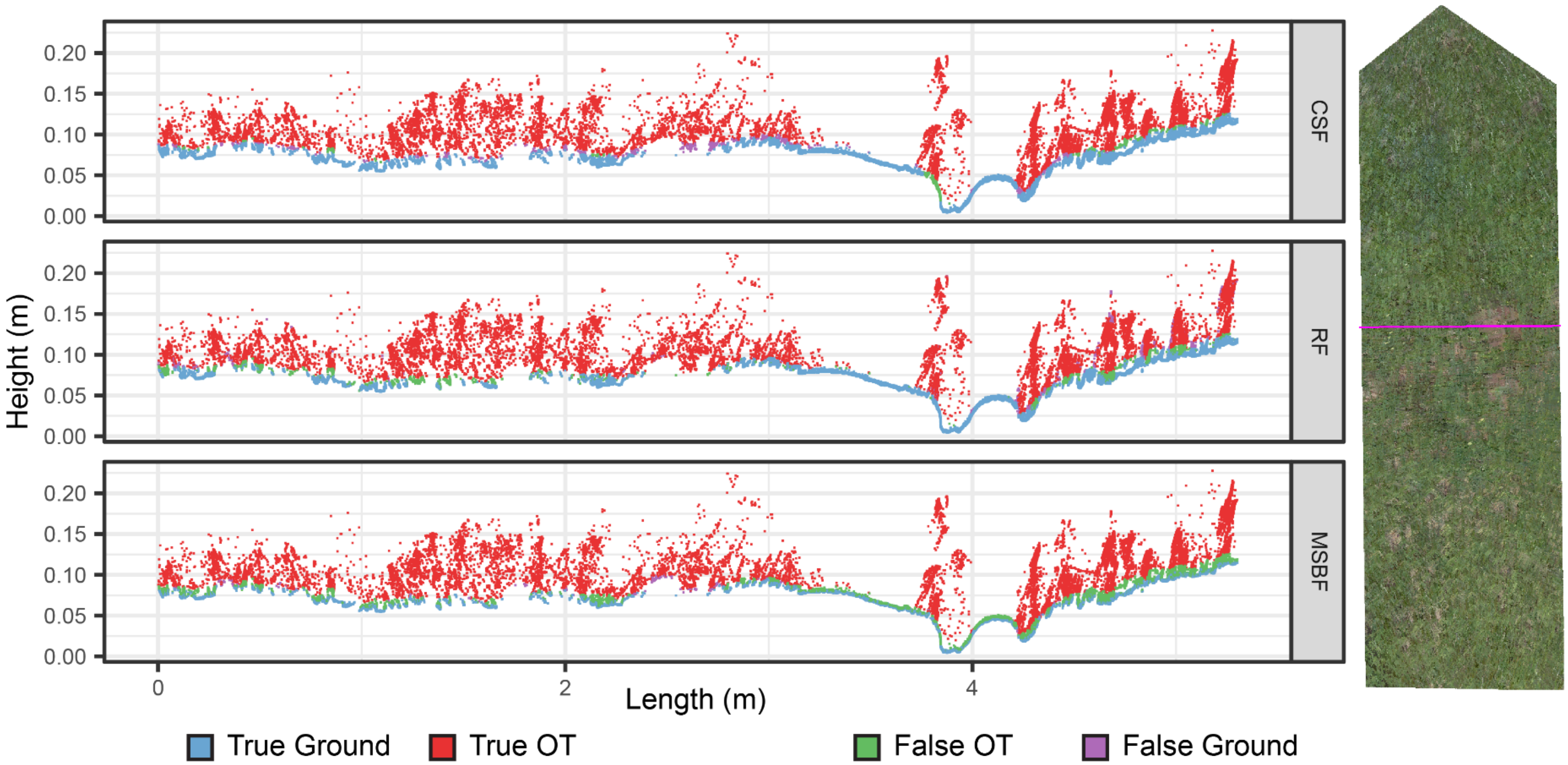


**Figure 18. Cross section with filtering results applied**

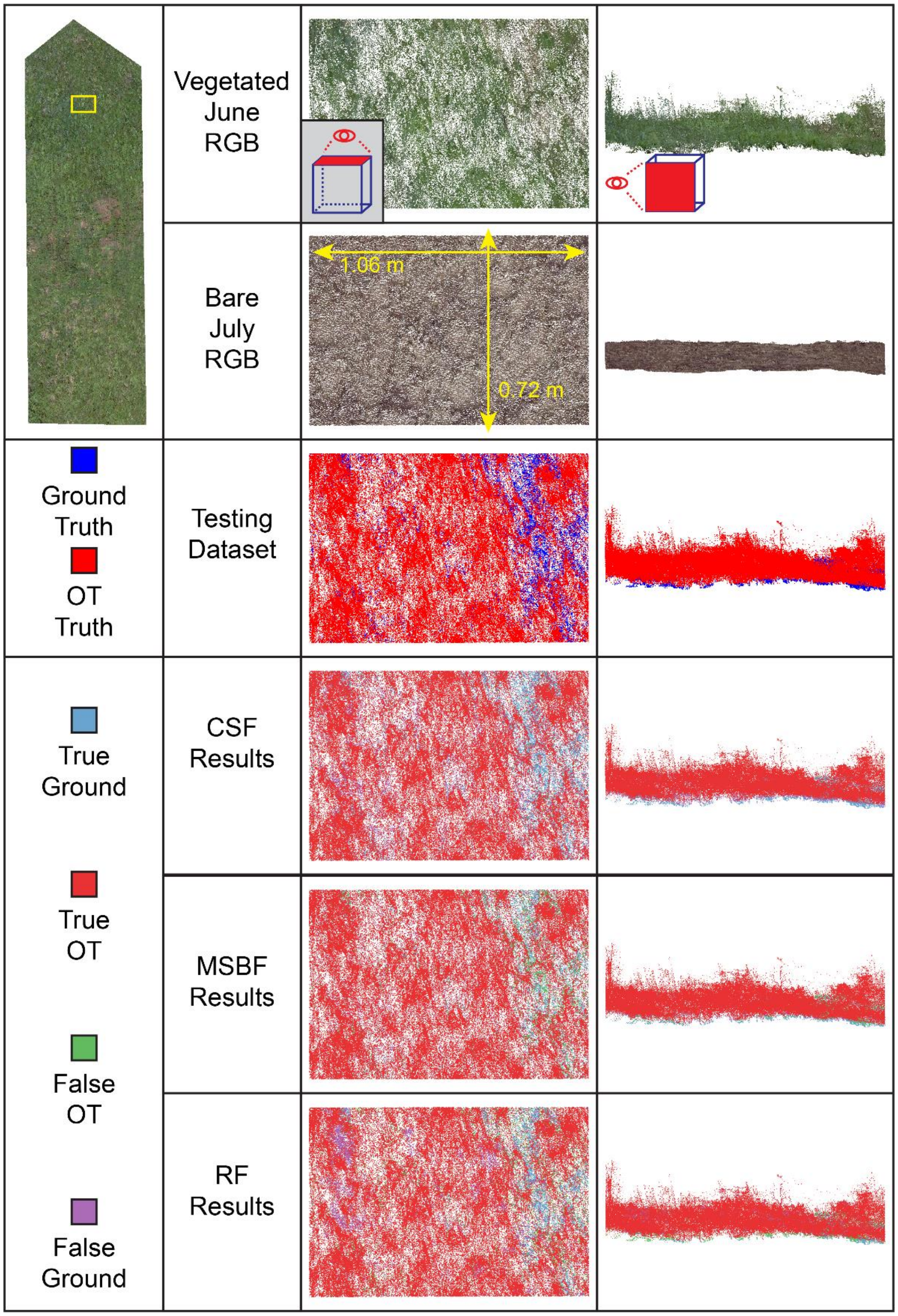


**Figure 19. Filtering results on a vegetated portion of the plot**

points as ground on the left portions of the site where the vegetation is thicker but to a lesser degree than RF. The RF classifier misclassifies points more frequently than the other algorithms in densely vegetated areas. The MSBF's high OT recall score suggests that the MSBF excels in this vegetated area, though the same pattern of disqualifying many ground points is still evident on the right portion of the area.

The area shown in Figure 20 contains a variety of conditions: taller, denser vegetation on the left, a single plant surrounded by flat ground in the center, and short vegetation close to ground on the right. The CSF and RF algorithms classify most flat ground and densely vegetated areas correctly. The MSBF algorithm again demonstrates the pattern of excessively excluding ground points. This site is notable in that it contains portions of the testing dataset that are incorrectly classified as OT but are not a result of vegetation or noise. When observing the RGB images of the upper right-hand corner and the ground surface to the right of the plant, it is clear that in these areas, neither scan included any vegetation, and the points' coherent pattern indicates no excessive noise. The surface of these areas moved at least a centimeter between the June and July scans due to erosion. Considering these areas where the testing data is incorrect, the CSF and MSBF algorithms classify the ground more accurately than they appear to at this site as they both classify the erroneous portions as ground. Interestingly, the RF classification agrees with the misclassified testing data, and this is evidence that the RF model fits tightly to its training data, suggesting that the RF implementation here is sensitive to the training data, and even the relatively few errors in our automatically generating testing dataset may be inappropriate to train RF models.

## Conclusions

This study used successive fine-resolution TLS scans of a hillslope plot before and after removing vegetation to generate an automatically classified testing dataset to assess the performance of three point cloud filtering methods: CSF, MSBF, and RF. The performance of each algorithm is affected by the selection of input parameters.

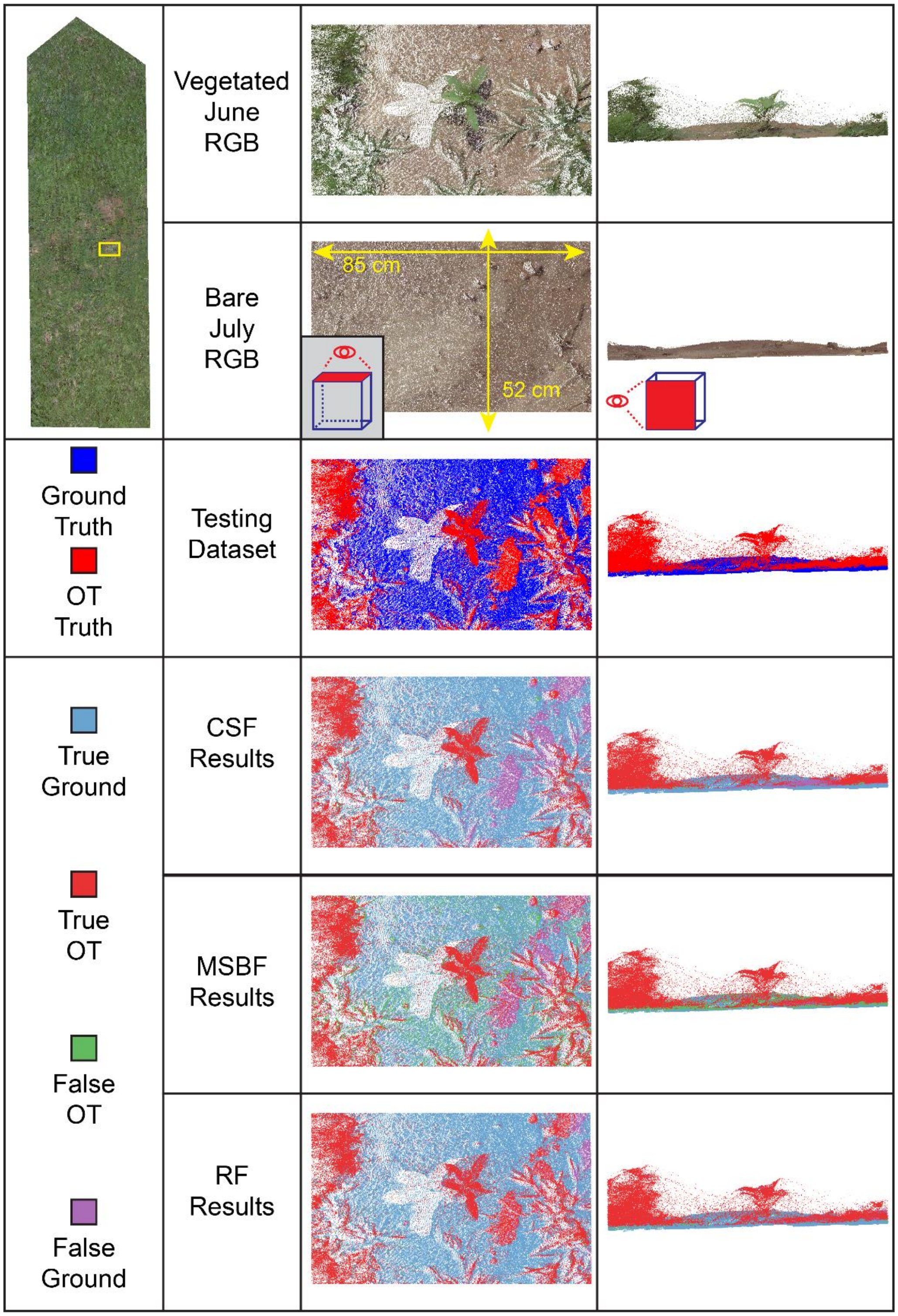


**Figure 20. Filtering results on a mixed portion of the plot**

The ‘time step’ parameter was highly influential over classification accuracy for the CSF algorithm. The default value for this parameter leads to the least accurate classifications, directly contradicting the recommendations of the algorithm’s authors. The variations of parameters for the MSBF algorithm produced a tighter—though less accurate—range of classification accuracies. The ‘slope threshold’ parameter showed the closest correlation with classification accuracy. Two RF models were tested considering 3 and 5 neighborhoods of eigenvalues, and RF classification accuracy increased with increasing numbers of neighborhoods.

When comparing classification accuracy, the CSF algorithm outperformed RF and MSBF. CSF scored higher in most metrics, including a Kappa score of 0.86 compared to 0.75 for RF and 0.62 for MSBF. Considering the classification metrics of CSF and the results of the parameter analysis, it is evident that although designed for airborne LiDAR data, CSF can produce highly accurate classification on TLS data when the parameters are carefully considered. Although it scored the lowest by Kappa score, the MSBF algorithm had the highest ground precision and OT recall score, suggesting that it may be advantageous when it is critical to capture only ground points at the cost of overkilling some ground points. In addition, spatial observations of MSBF displayed a pattern of falsely identifying ground points as OT in locations where the points were slightly above an otherwise relatively flat area. The RF model produced moderately successful classifications despite being trained using only fifteen features. This study suggests that the performance of filtering algorithms varies depending on input parameters. An in-depth parameter sensitivity analysis may further extend the applications of automatic filtering algorithms in TLS data.

It should be noted that the testing dataset automatically developed and implemented here is not perfect. Because the plot experienced some natural rainfall and erosion while vegetation was being removed between the two scans, it is hard to conclude that differences between the point clouds result from the presence of OT points alone. A 1 cm distance threshold was used to classify the testing dataset to mitigate the effects of erosion. Despite this, misclassified points can be observed in one of the visualized sites.

Future studies may consider applying these filtering and parameters to smaller samples of manually classified TLS testing datasets.

# CONCLUSION

This work presents two papers addressing specific difficulties encountered when measuring small-scale hillslope erosion using terrestrial LiDAR. The first article presented a new method for conducting uncertainty testing. This new method, Las2DoD, utilizes a cell-by-cell Welch's *t*-test conducted using only positional information inherent to the point clouds. In a case study estimating sediment delivery of a hillslope plot using terrestrial LiDAR, the Las2DoD method outperformed a minimum detection threshold and the multi-scale model to model comparison method. The Las2DoD method of uncertainty testing is advantageous when the magnitude of expected changes on a surface is relatively small and the point clouds are dense.

The second article analyzes the performance of three point cloud filtering algorithms: an algorithm based on cloth simulation, a slope-based algorithm, and a random forest classifier. All were tested on datasets generated using high-density TLS data. An automatically classified testing dataset of over 30 million points was created through a cloud-to-cloud distance analysis of LiDAR scans of the study site before and after removing dense vegetation. This data subset of the data provided the random forest classifier training data and served as a classification benchmark for all three algorithms. Many sets of input parameters for the cloth and slope-based algorithms and two models for the random forest algorithm were analyzed using the testing dataset.

The highest performing algorithm implementations on the subset were then compared to one another for the full dataset. The cloth simulation algorithm produced the highest accuracy classification with a 0.86 Kappa score, although its parameters need to be carefully considered, as the default parameters and recommendations for the cloth simulation algorithm yielded poor classifications. The slope-based algorithm produced the lowest Kappa score of the three algorithms but was exceptionally accurate in classifying ground points. The random forest classifier was moderately successful, and the inclusion of more training features was shown to improve performance despite both models being built on relatively few training features.

The TLS data used in this work contained a mean absolute registration error of 3.5 mm, though it is reasonable to see this as a pessimistic value. As the first step in processing most LiDAR data, point cloud registration influences all further processing. Future work should seek to lower this error as much as possible, especially considering the extreme precision required in estimating small scale erosion. The Las2DoD uncertainty analysis method presented in the first chapter was developed and tested on TLS data gathered in optimal conditions and did not account for any systematic errors inherent to the point cloud. Further testing of Las2DoD should incorporate different sites under different conditions and with different sensors. The testing dataset generated in the second chapter contained some falsely classified points due to the small amount of rainfall on the study site between vegetated and bare scans. While the misclassifications appear to be a tiny portion of the over 30 million points, and two of the three algorithms identified the misclassified points, it would be worthwhile to see if the results can be replicated on a more controlled testing dataset.

The articles presented here both take essential steps towards discovering the detection limit of terrestrial LiDAR for measuring hillslope erosion. By improving uncertainty analysis methods in analyzing surface changes and providing comparisons of filtering algorithms on dense point clouds, this work will support future efforts to extend the capabilities of the terrestrial LiDAR system.

# REFERENCES

1. Tóth, G.; Gardi, C.; Bódis, K.; Ivits, É.; Aksoy, E.; Jones, A.; Jeffrey, S.; Petursdottir, T.; Montanarella, L. Continental-Scale Assessment of Provisioning Soil Functions in Europe. *Ecol Process* **2013**, *2*, 32, doi:10.1186/2192-1709-2-32.
2. Montanarella, L.; Pennock, D.J.; McKenzie, N.; Badraoui, M.; Chude, V.; Baptista, I.; Mamo, T.; Yemefack, M.; Singh Aulakh, M.; Yagi, K.; et al. World's Soils Are under Threat. *SOIL* **2016**, *2*, 79–82, doi:10.5194/soil-2-79-2016.
3. Montgomery, D.R. Soil Erosion and Agricultural Sustainability. *Proceedings of the National Academy of Sciences* **2007**, *104*, 13268–13272, doi:10.1073/pnas.0611508104.
4. Poesen, J. Soil Erosion in the Anthropocene: Research Needs: Soil Erosion in the Anthropocene. *Earth Surf. Process. Landforms* **2018**, *43*, 64–84, doi:10.1002/esp.4250.
5. Nouwakpo, S.K.; Williams, C.J.; Al-Hamdan, O.Z.; Weltz, M.A.; Pierson, F.; Nearing, M. A Review of Concentrated Flow Erosion Processes on Rangelands: Fundamental Understanding and Knowledge Gaps. *International Soil and Water Conservation Research* **2016**, *4*, 75–86, doi:10.1016/j.iswcr.2016.05.003.
6. Young, R.A.; Wiersma, J.L. The Role of Rainfall Impact in Soil Detachment and Transport. *Water Resources Research* **1973**, *9*, 1629–1636, doi:10.1029/WR009i006p01629.
7. Govers, G.; Giménez, R.; Van Oost, K. Rill Erosion: Exploring the Relationship between Experiments, Modelling and Field Observations. *Earth-Science Reviews* **2007**, *84*, 87–102, doi:10.1016/j.earscirev.2007.06.001.
8. Poesen, J.; Nachtergaele, J.; Verstraeten, G.; Valentin, C. Gully Erosion and Environmental Change: Importance and Research Needs. *CATENA* **2003**, *50*, 91–133, doi:10.1016/S0341-8162(02)00143-1.
9. Bull, L.J.; Kirkby, M.J. Gully Processes and Modelling. *Progress in Physical Geography: Earth and Environment* **1997**, *21*, 354–374, doi:10.1177/030913339702100302.
10. Bilotta, G.S.; Grove, M.; Mudd, S.M. Assessing the Significance of Soil Erosion. *Transactions of the Institute of British Geographers* **2012**, *37*, 342–345.
11. de Vente, J.; Poesen, J.; Verstraeten, G.; Govers, G.; Vanmaercke, M.; Van Rompaey, A.; Arabkhedri, M.; Boix-Fayos, C. Predicting Soil Erosion and Sediment Yield at Regional Scales: Where Do We Stand? *Earth-Science Reviews* **2013**, *127*, 16–29, doi:10.1016/j.earscirev.2013.08.014.
12. Toy, T.J.; Foster, G.R.; Renard, K.G. *Soil Erosion: Processes, Prediction, Measurement, and Control*; John Wiley & Sons, 2002; ISBN 978-0-471-38369-7.
13. Verheijen, F.G.A.; Jones, R.J.A.; Rickson, R.J.; Smith, C.J. Tolerable versus Actual Soil Erosion Rates in Europe. *Earth-Science Reviews* **2009**, *94*, 23–38, doi:10.1016/j.earscirev.2009.02.003.
14. Boardman, J. Soil Erosion Science: Reflections on the Limitations of Current Approaches. *CATENA* **2006**, *68*, 73–86, doi:10.1016/j.catena.2006.03.007.

15. García-Ruiz, J.M.; Beguería, S.; Nadal-Romero, E.; González-Hidalgo, J.C.; Lana-Renault, N.; Sanjuán, Y. A Meta-Analysis of Soil Erosion Rates across the World. *Geomorphology* **2015**, *239*, 160–173, doi:10.1016/j.geomorph.2015.03.008.
16. Mutchler, C.K. *Runoff Plot Design and Installation for Soil Erosion Studies*; Agricultural Research Service, United States Department of Agriculture, 1963;
17. Evans, R. An Alternative Way to Assess Water Erosion of Cultivated Land – Field-Based Measurements: And Analysis of Some Results. *Applied Geography* **2002**, *22*, 187–207, doi:10.1016/S0143-6228(02)00004-8.
18. Hudson, N.; Nations, F. and A.O. of the U. *Field Measurement of Soil Erosion and Runoff*; Food & Agriculture Org., 1993; ISBN 978-92-5-103406-4.
19. Wischmeier, W.H.; Smith, D.D. *Predicting Rainfall Erosion Losses: A Guide to Conservation Planning*; Department of Agriculture, Science and Education Administration, 1978;
20. Evans, R.; Brazier, R. Evaluation of Modelled Spatially Distributed Predictions of Soil Erosion by Water versus Field-Based Assessments. *Environmental Science & Policy* **2005**, *8*, 493–501, doi:10.1016/j.envsci.2005.04.009.
21. Laflen, J.M.; Lane, L.J.; Foster, G.R. WEPP: A New Generation of Erosion Prediction Technology. *Journal of Soil and Water Conservation* **1991**, *46*, 34–38.
22. Boardman, J. The Challenge of Soil Erosion: Where Do We Now Stand? *International Journal of Environmental Sciences & Natural Resources* **2018**, *15*, 24–26.
23. Leopold, L.B. *Channel and Hillslope Processes in a Semiarid Area, New Mexico*; U.S. Government Printing Office, 1966;
24. Vandekerckhove, L.; Poesen, J.; Oostwoud Wijdenes, D.; Gyssels, G. Short-Term Bank Gully Retreat Rates in Mediterranean Environments. *CATENA* **2001**, *44*, 133–161, doi:10.1016/S0341-8162(00)00152-1.
25. Wijdenes, D.J.O.; Bryan, R. Gully-Head Erosion Processes on a Semi-Arid Valley Floor in Kenya: A Case Study into Temporal Variation and Sediment Budgeting. *Earth Surface Processes and Landforms* **2001**, *26*, 911–933, doi:10.1002/esp.225.
26. Evans, R. Water Erosion in British Farmers' Fields- Some Causes, Impacts, Predictions. *Progress in Physical Geography: Earth and Environment* **1990**, *14*, 199–219, doi:10.1177/030913339001400203.
27. Govers, G.; Poesen, J. Assessment of the Interrill and Rill Contributions to Total Soil Loss from an Upland Field Plot. *Geomorphology* **1988**, *1*, 343–354, doi:10.1016/0169-555X(88)90006-2.
28. Parsons, A.J. How Reliable Are Our Methods for Estimating Soil Erosion by Water? *Science of The Total Environment* **2019**, *676*, 215–221, doi:10.1016/j.scitotenv.2019.04.307.
29. Jester, W.; Klik, A. Soil Surface Roughness Measurement—Methods, Applicability, and Surface Representation. *CATENA* **2005**, *64*, 174–192, doi:10.1016/j.catena.2005.08.005.
30. Berger, C.; Schulze, M.; Rieke-Zapp, D.; Schlunegger, F. Rill Development and Soil Erosion: A Laboratory Study of Slope and Rainfall Intensity. *Earth Surface*

*Processes and Landforms* **2010**, *35*, 1456–1467, doi:https://doi.org/10.1002/esp.1989.

31. Marzolff, I.; Poesen, J. The Potential of 3D Gully Monitoring with GIS Using High-Resolution Aerial Photography and a Digital Photogrammetry System. *Geomorphology* **2009**, *111*, 48–60, doi:10.1016/j.geomorph.2008.05.047.
32. Westoby, M.J.; Brasington, J.; Glasser, N.F.; Hambrey, M.J.; Reynolds, J.M. 'Structure-from-Motion' Photogrammetry: A Low-Cost, Effective Tool for Geoscience Applications. *Geomorphology* **2012**, *179*, 300–314, doi:10.1016/j.geomorph.2012.08.021.
33. Hänsel, P.; Schindewolf, M.; Eltner, A.; Kaiser, A.; Schmidt, J. Feasibility of High-Resolution Soil Erosion Measurements by Means of Rainfall Simulations and SfM Photogrammetry. *Hydrology* **2016**, *3*, 38, doi:10.3390/hydrology3040038.
34. Javernick, L.; Brasington, J.; Caruso, B. Modeling the Topography of Shallow Braided Rivers Using Structure-from-Motion Photogrammetry. *Geomorphology* **2014**, *213*, 166–182, doi:10.1016/j.geomorph.2014.01.006.
35. Nouwakpo, S.K.; Weltz, M.A.; McGwire, K. Assessing the Performance of Structure-from-Motion Photogrammetry and Terrestrial LiDAR for Reconstructing Soil Surface Microtopography of Naturally Vegetated Plots. *Earth Surface Processes and Landforms* **2016**, *41*, 308–322, doi:10.1002/esp.3787.
36. Meinen, B.U.; Robinson, D.T. Where Did the Soil Go? Quantifying One Year of Soil Erosion on a Steep Tile-Drained Agricultural Field. *Science of The Total Environment* **2020**, *729*, 138320, doi:10.1016/j.scitotenv.2020.138320.
37. Kaiser, A.; Erhardt, A.; Eltner, A. Addressing Uncertainties in Interpreting Soil Surface Changes by Multitemporal High-Resolution Topography Data across Scales. *Land Degrad Dev* **2018**, *29*, 2264–2277, doi:10.1002/ldr.2967.
38. Eltner, A.; Schneider, D.; Maas, H.-G. INTEGRATED PROCESSING OF HIGH RESOLUTION TOPOGRAPHIC DATA FOR SOIL EROSION ASSESSMENT CONSIDERING DATA ACQUISITION SCHEMES AND SURFACE PROPERTIES. *Int. Arch. Photogramm. Remote Sens. Spatial Inf. Sci.* **2016**, *XLI-B5*, 813–819, doi:10.5194/isprsarchives-XLI-B5-813-2016.
39. Neugirg, F.; Stark, M.; Kaiser, A.; Vlacilova, M.; Della Seta, M.; Vergari, F.; Schmidt, J.; Becht, M.; Haas, F. Erosion Processes in Calanchi in the Upper Orcia Valley, Southern Tuscany, Italy Based on Multitemporal High-Resolution Terrestrial LiDAR and UAV Surveys. *Geomorphology* **2016**, *269*, 8–22, doi:10.1016/j.geomorph.2016.06.027.
40. Lefsky, M.A.; Cohen, W.B.; Parker, G.G.; Harding, D.J. Lidar Remote Sensing for Ecosystem StudiesLidar, an Emerging Remote Sensing Technology That Directly Measures the Three-Dimensional Distribution of Plant Canopies, Can Accurately Estimate Vegetation Structural Attributes and Should Be of Particular Interest to Forest, Landscape, and Global Ecologists. *BioScience* **2002**, *52*, 19–30, doi:10.1641/0006-3568(2002)052[0019:LRSFES]2.0.CO;2.

41. Perroy, R.L.; Bookhagen, B.; Asner, G.P.; Chadwick, O.A. Comparison of Gully Erosion Estimates Using Airborne and Ground-Based LiDAR on Santa Cruz Island, California. *Geomorphology* **2010**, *118*, 288–300, doi:10.1016/j.geomorph.2010.01.009.
42. Höfle, B.; Griesbaum, L.; Forbriger, M. GIS-Based Detection of Gullies in Terrestrial LiDAR Data of the Cerro Llamoca Peatland (Peru). *Remote Sensing* **2013**, *5*, 5851–5870, doi:10.3390/rs5115851.
43. Li, Y.; McNelis, J.J.; Washington-Allen, R.A. Quantifying Short-Term Erosion and Deposition in an Active Gully Using Terrestrial Laser Scanning: A Case Study From West Tennessee, USA. *Frontiers in Earth Science* **2020**, *8*, 14.
44. Goodwin, N.R.; Armston, J.D.; Muir, J.; Stiller, I. Monitoring Gully Change: A Comparison of Airborne and Terrestrial Laser Scanning Using a Case Study from Aratula, Queensland. *Geomorphology* **2017**, *282*, 195–208, doi:10.1016/j.geomorph.2017.01.001.
45. Lu, X.; Li, Y.; Washington-Allen, R.A.; Li, Y. Structural and Sedimentological Connectivity on a Rilled Hillslope. *Science of The Total Environment* **2019**, *655*, 1479–1494, doi:10.1016/j.scitotenv.2018.11.137.
46. Lu, X.; Li, Y.; Washington-Allen, R.A.; Li, Y.; Li, H.; Hu, Q. The Effect of Grid Size on the Quantification of Erosion, Deposition, and Rill Network. *International Soil and Water Conservation Research* **2017**, *5*, 241–251, doi:10.1016/j.iswcr.2017.06.002.
47. Eltner, A.; Baumgart, P. Accuracy Constraints of Terrestrial Lidar Data for Soil Erosion Measurement: Application to a Mediterranean Field Plot. *Geomorphology* **2015**, *245*, 243–254, doi:10.1016/j.geomorph.2015.06.008.
48. Rengers, F.K.; Tucker, G.E. The Evolution of Gully Headcut Morphology: A Case Study Using Terrestrial Laser Scanning and Hydrological Monitoring. *Earth Surface Processes and Landforms* **2015**, *40*, 1304–1317, doi:10.1002/esp.3721.
49. Vericat, D.; Smith, M.W.; Brasington, J. Patterns of Topographic Change in Sub-Humid Badlands Determined by High Resolution Multi-Temporal Topographic Surveys. *CATENA* **2014**, *120*, 164–176, doi:10.1016/j.catena.2014.04.012.
50. Liu, J.; Liang, X.; Hyyppä, J.; Yu, X.; Lehtomäki, M.; Pyörälä, J.; Zhu, L.; Wang, Y.; Chen, R. Automated Matching of Multiple Terrestrial Laser Scans for Stem Mapping without the Use of Artificial References. *International Journal of Applied Earth Observation and Geoinformation* **2017**, *56*, 13–23, doi:10.1016/j.jag.2016.11.003.
51. Day, S.S.; Gran, K.B.; Belmont, P.; Wawrzyniec, T. Measuring Bluff Erosion Part 1: Terrestrial Laser Scanning Methods for Change Detection. *Earth Surface Processes and Landforms* **2013**, *38*, 1055–1067, doi:10.1002/esp.3353.
52. Lague, D.; Brodu, N.; Leroux, J. Accurate 3D Comparison of Complex Topography with Terrestrial Laser Scanner: Application to the Rangitikei Canyon (N-Z). *ISPRS Journal of Photogrammetry and Remote Sensing* **2013**, *82*, 10–26, doi:10.1016/j.isprsjprs.2013.04.009.

53. Cheng, L.; Chen, S.; Liu, X.; Xu, H.; Wu, Y.; Li, M.; Chen, Y. Registration of Laser Scanning Point Clouds: A Review. *Sensors* **2018**, *18*, 1641, doi:10.3390/s18051641.
54. Franaszek, M.; Cheok, G.S.; Witzgall, C. Fast Automatic Registration of Range Images from 3D Imaging Systems Using Sphere Targets. *Automation in Construction* **2009**, *18*, 265–274, doi:10.1016/j.autcon.2008.08.003.
55. Wheaton, J.M.; Brasington, J.; Darby, S.E.; Sear, D.A. Accounting for uncertainty in DEMs from repeat topographic surveys: improved sediment budgets. *Earth Surface Processes and Landforms* **2010**, *35*, 136–156, doi:https://doi.org/10.1002/esp.1886.
56. Lechner, A.M.; Jones, S.D.; Bekessy, S.A. A Study on the Impact of Scale-Dependent Factors on the Classification of Landcover Maps. **2008**.
57. Schürch, P.; Densmore, A.L.; Rosser, N.J.; Lim, M.; McArdell, B.W. Detection of Surface Change in Complex Topography Using Terrestrial Laser Scanning: Application to the Illgraben Debris-Flow Channel. *Earth Surface Processes and Landforms* **2011**, *36*, 1847–1859, doi:https://doi.org/10.1002/esp.2206.
58. Girardeau-Montaut, D.; Roux, M.; Marc, R.; Thibault, G. Change Detection on Points Cloud Data Acquired with a Ground Laser Scanner, Laser Scanning 2005. In Proceedings of the ISPRS Workshop, Enschede, the Netherlands; 2005.
59. Nourbakhshbeidokhti, S.; Kinoshita, A.; Chin, A.; Florsheim, J. A Workflow to Estimate Topographic and Volumetric Changes and Errors in Channel Sedimentation after Disturbance. *Remote Sensing* **2019**, *11*, 586, doi:10.3390/rs11050586.
60. Barneveld, R.J.; Seeger, M.; Maalen-Johansen, I. Assessment of Terrestrial Laser Scanning Technology for Obtaining High-Resolution DEMs of Soils: TLS FOR HIGH-RESOLUTION DEMS. *Earth Surf. Process. Landforms* **2013**, *38*, 90–94, doi:10.1002/esp.3344.
61. Meng, X.; Currit, N.; Zhao, K. Ground Filtering Algorithms for Airborne LiDAR Data: A Review of Critical Issues. *Remote Sensing* **2010**, *2*, 833–860, doi:10.3390/rs2030833.
62. Brodu, N.; Lague, D. 3D Terrestrial Lidar Data Classification of Complex Natural Scenes Using a Multi-Scale Dimensionality Criterion: Applications in Geomorphology. *ISPRS Journal of Photogrammetry and Remote Sensing* **2012**, *68*, 121–134, doi:10.1016/j.isprsjprs.2012.01.006.
63. Rusu, R.B.; Cousins, S. 3D Is Here: Point Cloud Library (PCL). In Proceedings of the 2011 IEEE International Conference on Robotics and Automation; May 2011; pp. 1–4.
64. Che, E.; Olsen, M.J. Fast Ground Filtering for TLS Data via Scanline Density Analysis. *ISPRS Journal of Photogrammetry and Remote Sensing* **2017**, *129*, 226–240, doi:10.1016/j.isprsjprs.2017.05.006.
65. Zhang, W.; Qi, J.; Wan, P.; Wang, H.; Xie, D.; Wang, X.; Yan, G. An Easy-to-Use Airborne LiDAR Data Filtering Method Based on Cloth Simulation. *Remote Sensing* **2016**, *8*, 501, doi:10.3390/rs8060501.

66. Vosselman, G. Slope Based Filtering of Laser Altimetry Data. *IAPRS* **2000**, *XXXIII*.
67. Sithole, G.; Vosselman, G. Experimental Comparison of Filter Algorithms for Bare-Earth Extraction from Airborne Laser Scanning Point Clouds. *ISPRS Journal of Photogrammetry and Remote Sensing* **2004**, *59*, 85–101, doi:10.1016/j.isprsjprs.2004.05.004.
68. Haralick, R.M.; Shapiro, L.G. *Computer and Robot Vision*; Addison-wesley Reading, 1992; Vol. 1;.
69. Kilian, J.; Haala, N.; Englich, M.; Iii, C. Capture Andevaluation of Airborne Laser Scanner Data. **2001**.
70. Zhang, K.; Shu-Ching, C.; Whitman, D.; Mei-Ling Shyu; Jianhua Yan; Chengcui Zhang A Progressive Morphological Filter for Removing Nonground Measurements from Airborne LIDAR Data. *IEEE Transactions on Geoscience and Remote Sensing* **2003**, *41*, 872–882, doi:10.1109/TGRS.2003.810682.
71. Roberts, K.C.; Lindsay, J.B.; Berg, A.A. An Analysis of Ground-Point Classifiers for Terrestrial LiDAR. *Remote Sensing* **2019**, *11*, 1915, doi:10.3390/rs11161915.
72. Tarolli, P. High-Resolution Topography for Understanding Earth Surface Processes: Opportunities and Challenges. *Geomorphology* **2014**, *216*, 295–312, doi:10.1016/j.geomorph.2014.03.008.
73. Tarolli, P.; Dalla Fontana, G. Hillslope-to-Valley Transition Morphology: New Opportunities from High Resolution DTMs. *Geomorphology* **2009**, *113*, 47–56, doi:10.1016/j.geomorph.2009.02.006.
74. Slatton, K.C.; Carter, W.E.; Shrestha, R.L.; Dietrich, W. Airborne Laser Swath Mapping: Achieving the Resolution and Accuracy Required for Geosurficial Research. *Geophysical Research Letters* **2007**, *34*, L23S10, doi:10.1029/2007GL031939.
75. Lu, X.; Li, Y.; Washington-Allen, R.A.; Li, Y.; Li, H.; Hu, Q. The Effect of Grid Size on the Quantification of Erosion, Deposition, and Rill Network. *International Soil and Water Conservation Research* **2017**, *5*, 241–251, doi:10.1016/j.iswcr.2017.06.002.
76. Lu, X.; Li, Y.; Washington-Allen, R.A.; Li, Y. Structural and Sedimentological Connectivity on a Rilled Hillslope. *Science of The Total Environment* **2019**, *655*, 1479–1494, doi:10.1016/j.scitotenv.2018.11.137.
77. Li, Y.; Lu, X.; Washington-Allen, R.A.; Li, Y. Microtopographic Controls on Erosion and Deposition of a Rilled Hillslope in Eastern Tennessee, USA. *Remote Sensing* **2022**, *14*, 1315, doi:10.3390/rs14061315.
78. Cândido, B.M.; Quinton, J.N.; James, M.R.; Silva, M.L.N.; de Carvalho, T.S.; de Lima, W.; Beniaich, A.; Eltner, A. High-Resolution Monitoring of Diffuse (Sheet or Interrill) Erosion Using Structure-from-Motion. *Geoderma* **2020**, *375*, 114477, doi:10.1016/j.geoderma.2020.114477.
79. Bolkas, D.; Naberezny, B.; Jacobson, M.G. Comparison of SUAS Photogrammetry and TLS for Detecting Changes in Soil Surface Elevations Following Deep

Tillage. *Journal of Surveying Engineering* **2021**, *147*, 04021001, doi:10.1061/(ASCE)SU.1943-5428.0000346.
80. Meijer, A.D.; Heitman, J.L.; White, J.G.; Austin, R.E. Measuring Erosion in Long-Term Tillage Plots Using Ground-Based Lidar. *Soil and Tillage Research* **2013**, *126*, 1–10, doi:10.1016/j.still.2012.07.002.
81. Turunen, M.; Turtola, E.; Vaaja, M.T.; Hyväluoma, J.; Koivusalo, H. Terrestrial Laser Scanning Data Combined with 3D Hydrological Modeling Decipher the Role of Tillage in Field Water Balance and Runoff Generation. *CATENA* **2020**, *187*, 104363, doi:10.1016/j.catena.2019.104363.
82. James, M.R.; Robson, S. Straightforward Reconstruction of 3D Surfaces and Topography with a Camera: Accuracy and Geoscience Application. *Journal of Geophysical Research: Earth Surface* **2012**, *117*, doi:10.1029/2011JF002289.
83. Prosdocimi, M.; Calligaro, S.; Sofia, G.; Dalla Fontana, G.; Tarolli, P. Bank Erosion in Agricultural Drainage Networks: New Challenges from Structure-from-Motion Photogrammetry for Post-Event Analysis. *Earth Surface Processes and Landforms* **2015**, *40*, 1891–1906, doi:10.1002/esp.3767.
84. Whitehead, K.; Moorman, B.J.; Hugenholtz, C.H. Brief Communication: Low-Cost, on-Demand Aerial Photogrammetry for Glaciological Measurement. *The Cryosphere* **2013**, *7*, 1879, doi:http://dx.doi.org/10.5194/tc-7-1879-2013.
85. Cook, K.L. An Evaluation of the Effectiveness of Low-Cost UAVs and Structure from Motion for Geomorphic Change Detection. *Geomorphology* **2017**, *278*, 195–208, doi:10.1016/j.geomorph.2016.11.009.
86. Girardeau-Montaut, D.; Roux, M.; Marc, R.; Thibault, G. Change Detection on Point Cloud Data Acquired with a Ground Laser Scanner. *International Archives of Photogrammetry, Remote Sensing and Spatial Information Sciences* **2005**, *36*.
87. Williams, R. DEMs of Difference. *Geomorphological Techniques* **2012**, *2*.
88. Brasington, J.; Rumsby, B.T.; McVey, R.A. Monitoring and modelling morphological change in a braided gravel-bed river using high resolution GPS-based survey. *Earth Surface Processes and Landforms* **2000**, *25*, 973–990, doi:10.1002/1096-9837(200008)25:9<973::AID-ESP111>3.0.CO;2-Y.
89. Wheaton, J.M. Uncertainty in Morphological Sediment Budgeting of Rivers. Ph.D., University of Southampton, 2008.
90. Blasone, G.; Cavalli, M.; Marchi, L.; Cazorzi, F. Monitoring Sediment Source Areas in a Debris-Flow Catchment Using Terrestrial Laser Scanning. *CATENA* **2014**, *123*, 23–36, doi:10.1016/j.catena.2014.07.001.
91. Croke, J.; Todd, P.; Thompson, C.; Watson, F.; Denham, R.; Khanal, G. The Use of Multi Temporal LiDAR to Assess Basin-Scale Erosion and Deposition Following the Catastrophic January 2011 Lockyer Flood, SE Queensland, Australia. *Geomorphology* **2013**, *184*, 111–126, doi:10.1016/j.geomorph.2012.11.023.
92. James, L.A.; Hodgson, M.E.; Ghoshal, S.; Latiolais, M.M. Geomorphic Change Detection Using Historic Maps and DEM Differencing: The Temporal Dimension

of Geospatial Analysis. *Geomorphology* **2012**, *137*, 181–198, doi:10.1016/j.geomorph.2010.10.039.
93. Brasington, J.; Langham, J.; Rumsby, B. Methodological Sensitivity of Morphometric Estimates of Coarse Fluvial Sediment Transport. *Geomorphology* **2003**, *53*, 299–316, doi:10.1016/S0169-555X(02)00320-3.
94. Lane, S.N.; Westaway, R.M.; Hicks, D.M. Estimation of erosion and deposition volumes in a large, gravel-bed, braided river using synoptic remote sensing. *Earth Surface Processes and Landforms* **2003**, *28*, 249–271, doi:10.1002/esp.483.
95. Welch, B.L. The Generalization of `Student's' Problem When Several Different Population Variances Are Involved. *Biometrika* **1947**, *34*, 28–35, doi:10.2307/2332510.
96. Bonilla, C.A.; Kroll, D.G.; Norman, J.M.; Yoder, D.C. Instrumentation for Measuring Runoff, Sediment, and Chemical Losses from Agricultural Fields. *Journal of Environmental Quality* **2006**, *35*, 216–223.
97. Hoomehr, S.; Schwartz, J.S.; Yoder, D.C.; Drumm, E.C.; Wright, W. Curve Numbers for Low-Compaction Steep-Sloped Reclaimed Mine Lands in the Southern Appalachians. *Journal of Hydrologic Engineering* **2013**, *18*, 1627–1638, doi:10.1061/(ASCE)HE.1943-5584.0000746.
98. Seo, Y.; Lee, J.; Hart, W.E.; Denton, H.P.; Yoder, D.C.; Essington, M.E.; Perfect, E. SEDIMENT LOSS AND NUTRIENT RUNOFF FROM THREE FERTILIZER APPLICATION METHODS. *Transactions of the ASAE* **2005**, *48*, 2155–2162, doi:10.13031/2013.20101.
99. Yoder, D.C.; Cope, T.L.; Wills, J.B.; Denton, H.P. No-till Transplanting of Vegetables and Tobacco to Reduce Erosion and Nutrient Surface Runoff. *Journal of Soil and Water Conservation* **2005**, *60*, 68–73.
100. Pinson, W.T.; Yoder, D.C.; Buchanan, J.R.; Wright, W.C.; Wilkerson, J.B. DESIGN AND EVALUATION OF AN IMPROVED FLOW DIVIDER FOR SAMPLING RUNOFF PLOTS. *APPLIED ENGINEERING IN AGRICULTURE* **2004**, *20*, 6.
101. Fan, L.; Smethurst, J.A.; Atkinson, P.M.; Powrie, W. Error in Target-Based Georeferencing and Registration in Terrestrial Laser Scanning. *Computers & Geosciences* **2015**, *83*, 54–64, doi:10.1016/j.cageo.2015.06.021.
102. Randrup, T.; Lichter, J. Measuring Soil Compaction on Construction Sites: A Review of Surface Nuclear Gauges and Penetrometers. *J. Arboric.* **2001**, *27*.
103. Rousseva, S.S.; Ahuja, L.R.; Heathman, G.C. Use of a Surface Gamma-Neutron Gauge for in Situ Measurement of Changes in Bulk Density of the Tilled Zone. *Soil and Tillage Research* **1988**, *12*, 235–251, doi:10.1016/0167-1987(88)90014-1.
104. Yang, R.; Meng, X.; Yao, Y.; Chen, B.Y.; You, Y.; Xiang, Z. An Analytical Approach to Evaluate Point Cloud Registration Error Utilizing Targets. *ISPRS Journal of Photogrammetry and Remote Sensing* **2018**, *143*, 48–56, doi:10.1016/j.isprsjprs.2018.05.002.

105. Weidner, L.; Walton, G.; Kromer, R. Generalization Considerations and Solutions for Point Cloud Hillslope Classifiers. *Geomorphology* **2020**, *354*, 107039, doi:10.1016/j.geomorph.2020.107039.
106. Lindsay, J.B. Whitebox GAT: A Case Study in Geomorphometric Analysis. *Computers & Geosciences* **2016**, *95*, 75–84, doi:10.1016/j.cageo.2016.07.003.
107. Pedregosa, F.; Varoquaux, G.; Gramfort, A.; Michel, V.; Thirion, B.; Grisel, O.; Blondel, M.; Prettenhofer, P.; Weiss, R.; Dubourg, V.; et al. Scikit-Learn: Machine Learning in Python. *J. Mach. Learn. Res.* **2011**, *12*, 2825–2830.
108. Cohen, J. A Coefficient of Agreement for Nominal Scales. *Educational and Psychological Measurement* **1960**, *20*, 37–46, doi:10.1177/001316446002000104.
109. McHugh, M.L. Interrater Reliability: The Kappa Statistic. *Biochem Med* **2012**, *22*, 276–282, doi:10.11613/BM.2012.031.

# VITA

Gene was born in East Tennessee and raised in Knoxville. He attended the University of Tennessee, where he received a Bachelor of Arts in Geography in 2015. Gene then worked at the Oak Ridge National Laboratory in the Geographic Information Science and Technology group until returning to the University of Tennessee in 2019 to earn a Master of Science in Geography under the advising of Dr. Yingkui Li. Gene's research interests include geomorphology, remote sensing, and geospatial programming.